

WINDS AS THE ORIGIN OF RADIO EMISSION IN $Z = 2.5$ RADIO-QUIET EXTREMELY RED QUASARS

HSIANG-CHIH HWANG¹, NADIA L. ZAKAMSKA¹, RACHAEL M. ALEXANDROFF^{2,3}, FRED HAMANN^{4,5}, JENNY E. GREENE⁶,
SERENA PERROTTA⁴, GORDON T. RICHARDS⁷

¹Department of Physics & Astronomy, Johns Hopkins University, Baltimore, MD 21218, USA

²Canadian Institute for Theoretical Astrophysics, The University of Toronto, Toronto, ON M5S 3H8, Canada

³Dunlap Institute for Astronomy and Astrophysics, The University of Toronto, Toronto, ON M5S 3H4, Canada

⁴Department of Physics and Astronomy, University of California, Riverside, CA 92507, USA

⁵Department of Astronomy, University of Florida, Gainesville, FL 32611, USA

⁶Department of Astrophysical Sciences, Princeton University, Princeton, NJ 08544, USA

⁷Department of Physics, Drexel University, Philadelphia, PA 19104, USA

ABSTRACT

Most active galactic nuclei (AGNs) are radio-quiet, and the origin of their radio emission is not well-understood. One hypothesis is that this radio emission is a by-product of quasar-driven winds. In this paper, we present the radio properties of 108 extremely red quasars (ERQs) at $z = 2 - 4$. ERQs are among the most luminous quasars ($L_{bol} \sim 10^{47-48} \text{ erg s}^{-1}$) in the Universe, with signatures of extreme ($\gg 1000 \text{ km s}^{-1}$) outflows in their [O III] $\lambda 5007 \text{ \AA}$ emission, making them the best subjects to seek the connection between radio and outflow activity. All ERQs but one are unresolved in the radio on $\sim 10 \text{ kpc}$ scales, and the median radio luminosity of ERQs is $\nu L_\nu [6 \text{ GHz}] = 10^{41.0} \text{ erg s}^{-1}$, in the radio-quiet regime, but one to two orders of magnitude higher than that of other quasar samples. The radio spectra are steep, with a mean spectral index $\langle \alpha \rangle = -1.0$. In addition, ERQs neatly follow the extrapolation of the low-redshift correlation between radio luminosity and the velocity dispersion of [O III]-emitting ionized gas. Uncollimated winds, with a power of one per cent of the bolometric luminosity, can account for all these observations. Such winds would interact with and shock the gas around the quasar and in the host galaxy, resulting in acceleration of relativistic particles and the consequent synchrotron emission observed in the radio. Our observations support the picture in which ERQs are signposts of extremely powerful episodes of quasar feedback, and quasar-driven winds as a contributor of the radio emission in the intermediate regime of radio luminosity $\nu L_\nu = 10^{39} - 10^{42} \text{ erg s}^{-1}$.

Keywords: galaxies: active – quasars: general – radio continuum: galaxies

1. INTRODUCTION

Since the discovery of the first radio quasar 3C 273, the shape of the radio luminosity function of active galactic nuclei (AGNs) has remained a topic of active research. Measurements of the radio luminosity function of AGNs are critically important for understanding which physical processes contribute to the radio emission. While several authors suggest that the radio luminosity function of AGN is bimodal (Kellermann et al. 1989; Xu et al. 1999; Ivezić et al. 2002), or at least cannot be fit by a unimodal distribution (Kratzer & Richards 2015), others find that the distribution of radio loudness indicators is instead continuous (White et al. 2000; Rafter et al. 2009; La Franca et al. 2010). Determining the shape of the luminosity function is important for discerning whether multiple mechanisms may be responsible for the radio emission in different luminosity

regimes. At a given AGN bolometric luminosity the radio power can span over six orders of magnitude – thus mapping the radio luminosity function of various AGN subpopulations remains difficult and requires deep radio observations to probe the faint end – the radio-quiet population.

While powerful jets dominate the bright radio sky (Urry & Padovani 1995), the radio-quiet population is still not well-understood. It is unclear whether star formation dominates the radio emission of radio-quiet AGNs (de Vries et al. 2007; Kimball et al. 2011; Condon et al. 2013; Kellermann et al. 2016) or whether it is insufficient and other mechanisms are required (Harrison et al. 2014; Rawlings et al. 2015; Zakamska et al. 2016b; Wang et al. 2017; White et al. 2017). It may be a function of the power of the active nucleus, with star formation dominating the radio emission in low-power

radio-quiet AGN (Rosario et al. 2013), but not in high-luminosity quasars (Zakamska et al. 2016b).

Other possible contributors to the radio-quiet population are compact or low-power jets launched by central supermassive black holes (Falcke et al. 2004; Leipski et al. 2006), secondary emission from quasar-driven winds (Stoche et al. 1992; Wang 2008; Jiang et al. 2010; Ishibashi & Courvoisier 2011; Faucher-Giguère & Quataert 2012; Zubovas & King 2012; Zakamska & Greene 2014; Nims et al. 2015), or coronal emission (Laor & Behar 2008; Raginski & Laor 2016). The recently uncovered correlation between the velocity width of forbidden emission lines and the radio power within the radio-quiet population suggests a connection between radio emission and quasar-driven winds on large scales (Mullaney et al. 2013; Zakamska & Greene 2014), making the secondary emission from quasar winds a particularly attractive possibility. In this picture, a wind produced on circumnuclear scales propagates into the surrounding interstellar medium and forms shocks which in turn generate relativistic electrons and the resulting synchrotron radiation.

The recently discovered population of extremely red quasars (ERQs) provides an excellent opportunity to test whether radio emission may be associated with quasar-driven winds. ERQs are selected by their high mid-infrared-to-optical ratios (Ross et al. 2015; Hamann et al. 2017). With $L_{\text{bol}} \sim 10^{47-48} \text{ erg s}^{-1}$, ERQs are among the most luminous quasars at the peak epoch of quasar and star formation activity at $z = 2 - 3$. Follow-up near-infrared spectroscopy of this population has revealed extremely broad and blueshifted $[\text{O III}]\lambda 5007 \text{ \AA}$ (hereafter $[\text{O III}]$) emission, indicating physical velocities of over 3000 km s^{-1} (Zakamska et al. 2016a; Perrotta et al. in prep). If these winds turn out to be spatially resolved on scales of a few kpc, they may represent the extreme end of galaxy-wide outflows detected in other quasars (Liu et al. 2013; Brusa et al. 2015; Perna et al. 2015; Carniani et al. 2015).

In this paper, we present the radio properties of 108 ERQs identified by Hamann et al. (2017). In Section 2 we describe our sample selection, observations, and data reduction. In Section 3 we present the measurements of radio flux densities, spectral indices, and radio luminosities of ERQs. In Section 4 we discuss the origin of radio emission in ERQs, and we conclude in Section 5. We use an $h = 0.7$, $\Omega_m = 0.3$, $\Omega_\Lambda = 0.7$ cosmology. We use SDSSJhhmm+ddmm notation for our ERQ targets throughout the text and the full Jhhmmss.ss+ddmmss.s notation in Table 4.

2. OBSERVATIONS AND DATA REDUCTION

2.1. Sample selection and observations

Extremely red quasars (ERQs; Hamann et al. 2017) at redshifts $z = 2.0 - 3.4$ are selected based on their high mid-infrared-to-optical ratios from optical and mid-infrared survey data. These sources are drawn from the Data Release 12 quasar catalog (DR12Q; Pâris et al. 2014, 2017) of the Baryon Oscillation Spectroscopic Survey (BOSS; Dawson et al. 2013) which is part of the Sloan Digital Sky Survey - III (SDSS; Eisenstein et al. 2011), while the infrared fluxes are from the all-sky data of the *Wide-field Infrared Survey Explorer* (*WISE*; Wright et al. 2010).

The main sample of 97 ERQs is selected using two criteria, and these ERQs constitute ~ 1.6 per cent of the number of luminous, blue quasars with similar redshifts and $W3$ magnitudes (Hamann et al. 2017). The first criterion is the red optical-to-mid-infrared color, specifically $i_{\text{AB}} - W3_{\text{AB}} > 4.6 \text{ mag}$ on the AB system where the i -band magnitudes are point-spread function magnitudes from SDSS Data Release 12 (Alam et al. 2015) and $W3$ is the $12 \mu\text{m}$ magnitude from *WISE*, with a conversion between AB and Vega system of $W3_{\text{AB}} = W3_{\text{Vega}} + 5.242$ (Cutri et al. 2011). The color cut alone selects a variety of interesting sources, including heavily reddened quasars, low-redshift type 2 quasars, and broad absorption line quasars (Ross et al. 2015). In addition, Hamann et al. (2017) also require that the rest equivalent width of $\text{C IV}\lambda 1548, 1551 \text{ \AA}$ (hereafter C IV) be greater than 100 \AA to preferentially select objects with suppressed continuum but strong emission lines, instead of normal quasars behind a dust reddening screen. To ensure robust measurements of emission line properties, sources with strong broad absorption features in C IV are excluded. The selection requirements do not change as a function of redshift, and as a result slightly different populations may be selected at different redshifts. In practice, 75 per cent of the sample is confined to a relatively narrow range in redshift from 2.2 to 2.6. ERQs in this paper are referred to ‘core’ ERQs in Hamann et al. (2017), but here we remove ‘core’ to avoid the confusion with the core in radio astronomy.

ERQs show peculiar properties including flat ultraviolet continua, wingless line shapes of C IV , and unusual line flux ratios such as $\text{N V}\lambda 1240 \text{ \AA} / \text{Ly } \alpha > 1$ and high $\text{N V} / \text{C IV}$. Expanding on these interesting features of the ERQ population, Hamann et al. (2017) investigate an additional 235 ERQ-like objects. For this sample, instead of using a color cut and a C IV rest equivalent width cut, Hamann et al. (2017) select objects with wingless C IV profiles and find that this population generally favors red $i - W3$ colors and high C IV equivalent widths, making them similar to ERQs. Hamann et al. (2017) suggest that the red colors of ERQs and their peculiar line properties might be related to powerful outflow activity and high accretion rates during a particular

early phase of quasar evolution.

In this paper, we investigate the radio properties of ERQs. Of the 97 ERQs, nine are detected at $F_\nu > 1$ mJy in the Faint Images of the Radio Sky at Twenty Centimeters (FIRST; Becker et al. 1995) survey, and their flux densities are listed in Table 1. We followed up the rest of the sample with sensitive radio observations using the Karl G. Jansky Very Large Array (VLA), but because the ERQ sample was still being finalized at the time, we targeted most ERQs and a few ERQ-like sources. Specifically, of the 88 ERQs without FIRST detections, 87 were observed while SDSSJ1212+5958 was not. In addition, we observed 14 ERQ-like objects, and one of them (SDSSJ1550+0806) is also detected in FIRST. SDSSJ1013+6112 matches all criteria of ERQs, but is listed in Hamann et al. (2017) as ERQ-like, and we keep this designation here.

Two FIRST-detected ERQs, SDSSJ0915+5613 and SDSSJ0950+2117, are targeted for follow-up spectroscopy with SDSS only because of their radio emission detected by FIRST. Including such objects in calculations of the radio luminosity function would bias our results, so we exclude these two sources from all statistical analysis, though they are listed in Table 1. Thus, our final sample consists of 108 objects with a median redshift of 2.53 – 7 FIRST-detected ERQs and 101 objects with targeted VLA observations of which 87 are ERQs and 14 are ERQ-like objects. The distribution in the color versus C IV equivalent width space of the final sample is shown in Figure 1. As is apparent from the Figure, although ERQ-like objects are selected based on C IV line shape, they also show the red colors and the high rest equivalent widths characteristic of the main ERQ sample, suggesting a strong connection between all these properties.

The observations were carried out using the VLA B configuration in the C-band (≈ 4 –8 GHz; Program 16A-108, PI: Zakamska), which provides a resolution of 1.3 arcsec, or ~ 10 kpc at $z = 2.5$. The full bandwidth is 4 GHz, with two basebands centered at 5.25 and 7.2 GHz respectively to avoid radio frequency interference between 4 and 4.2 GHz. All 101 objects were observed between June and August 2016 with 12 scheduling blocks. In each scheduling block, we started with a flux/bandpass calibrator, and after that gain calibrators and targets were observed alternately, with on-source time about 10 minutes for each target.

2.2. Data reduction

We reduce the radio data from the VLA with Common Astronomy Software Applications (CASA) package v.4.7.0 (McMullin et al. 2007). Raw visibilities are flagged and calibrated by the pipeline, and all calibration solutions are inspected and manually flagged

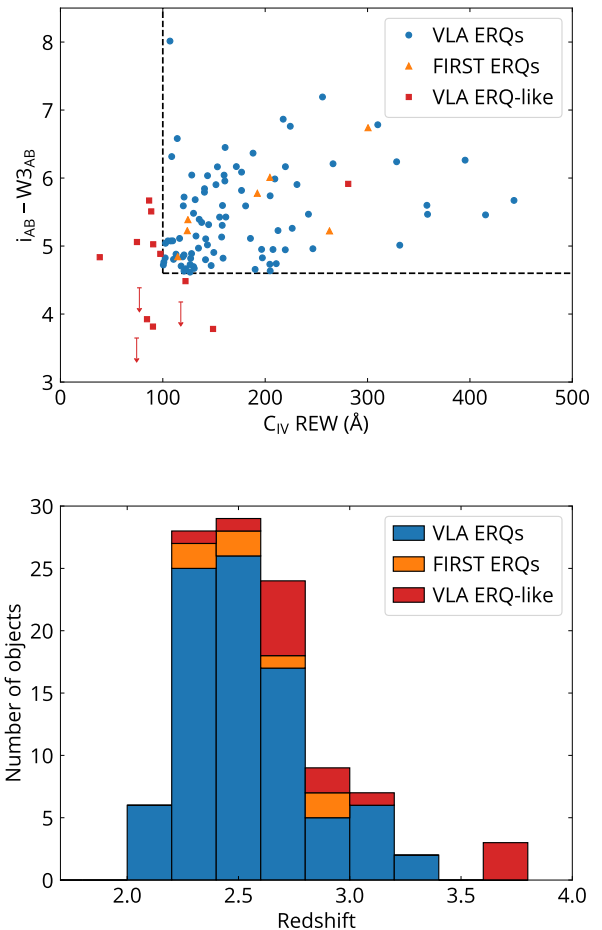


Figure 1. Colors and C IV rest equivalent widths (REWs) (top) and redshifts (bottom) for the final 108 ERQ sample discussed in this paper, including 94 ERQs and 14 ERQ-like objects. AB magnitude is used for i and $W3$. Blue dots are ERQs observed with VLA, orange triangles are ERQs detected in FIRST, and red squares represent ERQ-like objects. Three ERQ-like objects (SDSSJ0844+5452, SDSSJ1447+5652, and SDSSJ1629+4957) are not detected in $W3$, and their upper limits of $W3$ are set to $W3_{AB} = 17.3$, which is approximately the detection limit of $W3$ with a signal-to-noise ratio of 3. The dashed lines represent the selection criteria for ERQs, $i_{AB} - W3_{AB} > 4.6$ and rest equivalent width of C IV larger than 100 Å.

if needed. All images are cleaned with multi-frequency synthesis (MFS) mode with `nterms = 2`, which uses two terms in the Taylor expansion to model the sky spectrum and can reduce the artifacts due to wide-band imaging (Rau & Cornwell 2011). We automatically make circular cleaning masks with a radius of 4 arcsec for those sources detected in the FIRST catalog (Becker et al. 1995; White et al. 1997). After the first round of cleaning, we inspect the cleaned maps and add additional masks for objects below the detection limit of the FIRST catalog and adjust the size of the masks manually if necessary. The final image product is obtained by repeated

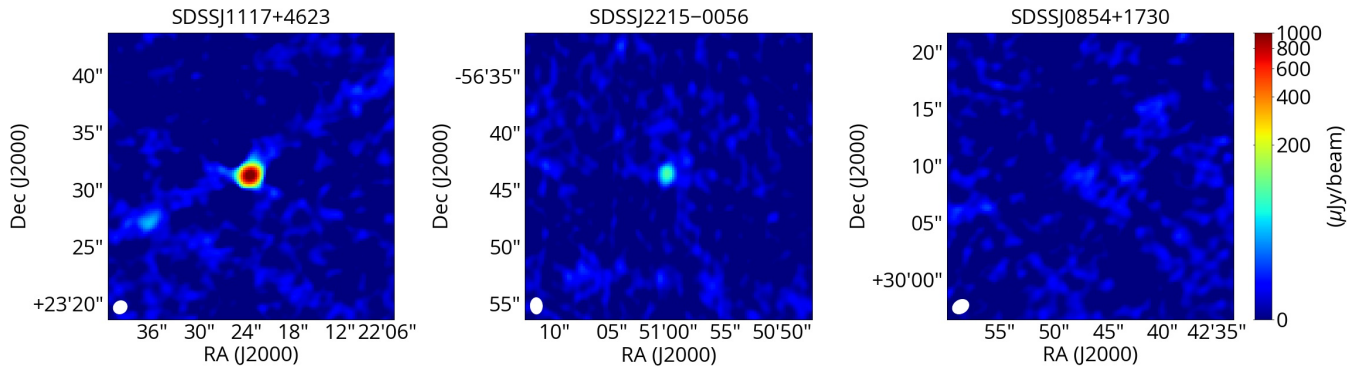


Figure 2. Three examples of cleaned images observed at 6.2 GHz with the full-width-at-half-maximum (FWHM) ellipse of the restoring beam shown in the lower left corner. Left: SDSSJ1117+4623, the brightest object with a flux density of 1.3 mJy in our VLA observations, with a beam of 1.27 arcsec \times 1.13 arcsec. A radio detection to the south-east does not have a counterpart in SDSS. It might be a ~ 80 kpc jet lobe of SDSSJ1117+4623, or an unrelated source. Middle: SDSSJ2215-0056, an ERQ with a flux density of $98 \mu\text{Jy}$, typical of the ERQ sample, also detected in Stripe 82 at 1.4 GHz. The size of the beam is 1.45 arcsec \times 1.06 arcsec. As most of ERQs, the source is unresolved. Right: SDSSJ0854+1730, one of the non-detected objects with a beam of 1.53 arcsec \times 1.18 arcsec. These three images share the same color scale, and therefore SDSSJ1117+4623 appears larger in the image due to extended wings of the Gaussian restoring beam, not because it is resolved.

cleaning and modifying masks several times (usually 3 to 5 times) until the regions within ~ 1 arcmin from our sources are free from dirty beams. In the meantime, we measure the root-mean-square noise level σ of the cleaned images, and the final images are cleaned down to 4σ , which is $\sim 30 \mu\text{Jy beam}^{-1}$ with a median noise level of $7.61 \mu\text{Jy beam}^{-1}$.

For each radio image, CASA provides a theoretically derived point spread function (PSF). During these steps, we confirm that all detected sources are unresolved at the resolution of ~ 1.3 arcsec, except SDSSJ1117+4623 discussed in Section 3.2. Given that all sources are located at the image center with negligible angular size compared to the primary beam, we do not perform primary beam correction for MFS mode. Example cleaned images are shown in Figure 2.

Because all sources (except one) are unresolved, we use natural weighting to maximize the sensitivity of cleaned maps to point sources. However, if there is a source brighter than ~ 100 mJy in the field (within ~ 8 arcmin), or brighter than 10 mJy and close to (within ~ 1 arcmin) the target source, the limit of dynamic range as well as the stronger sidelobes due to natural weighting prevent us from measuring the flux densities robustly. To mitigate this problem, four objects are imaged with Briggs weighting (ROBUST = 0.5 for SDSSJ0804+4701 and SDSSJ0935-0241, and ROBUST = 0.0 for SDSSJ0936+1019 and SDSSJ2203+1219), and additional phase and gain self-calibrations are applied to reach a higher dynamic range. Using Briggs weighting lowers the sensitivity to a point source, so we avoid its use except in these four cases where it is warranted by the contaminating artifacts.

2.3. Flux density measurement and CLEAN bias

To test the robustness of the flux density measurement, we insert an artificial point source in the central region of the field of SDSSJ1047+4844 with noise level $\sigma \sim 7 \mu\text{Jy beam}^{-1}$, where no source is detected within ~ 2 arcmin of the field center. For a specific flux density, we randomly place a point source at a distance less than 10 arcsec from the center, and measure the flux density using several methods after cleaning down to 4σ level with MFS mode of `nterms` = 2 and natural weighting, as described in Section 2.2. This routine is repeated 20 times for each flux density bin.

We present the results in Table 2, where we record five flux density measurements for the artificial sources. In the first method, we report the maximum pixel intensity of the source in units of $\mu\text{Jy beam}^{-1}$. In the other four methods, the source is fit with an elliptical two-dimensional Gaussian and we record its peak and integrated flux density (in $\mu\text{Jy beam}^{-1}$ and μJy , respectively) with and without an additional parameter for the background sky level. If the image is free from noise and sidelobes, fitted peak and integrated flux densities of a point source should all be the same, while the results of the first method may be different since it depends on the sampling position of sources.

We find that integrated flux densities usually overestimate the flux densities for a point source, which may be due to the uncleaned PSF under 4σ level. Peak flux densities with fitted sky level have the best performance. If the expected flux density is larger than $100 \mu\text{Jy}$, the measured peak flux density is accurate, with an average error equal to the noise level of the image. When the expected flux density is $50 \mu\text{Jy}$ ($\sim 7\sigma$), the measured peak flux density is overestimated by ~ 7 per cent.

We choose peak flux densities with fitted sky as our flux density measurement, appropriate since all sources

(except one) are unresolved. The measured flux densities of 101 objects are present in Table 4. In cases with stronger sidelobes from nearby bright sources, we carefully monitor the fitted sky level and ensure that the fitted integrated flux density is reasonably close to the value of fitted peak flux density.

Flux density measurements of snapshot radio data suffer from missing flux density during the cleaning process (Becker et al. 1995; White et al. 1997), so called CLEAN bias, which is not due to the undersampling resulting from incorrectly large pixel size nor the lack of spatial frequency coverage. The CLEAN bias is not well-understood, with listed values varying among different studies. White et al. (1997) show that CLEAN bias is independent of flux density of a source but dependent on the distance from the field center. In contrast, Hodge et al. (2011) find a flux density dependence in their CLEAN bias but do not see a distance dependence. In our test shown in Table 2, we do not see significant missing flux density. Rau et al. (2016) attribute the CLEAN bias to crowded fields and test the performance of several cleaning modes, showing that either the use of the cleaning masks or of the MFS mode is able to eliminate the effect. In this paper, we use both cleaning masks and MFS mode, which may be the reason that we do not see a CLEAN bias and therefore we do not apply any bias correction to our flux densities.

2.4. Measurements of spectral indices

Depending on the flux densities, we use some of the following five methods to measure the spectral indices α , defined as $F_\nu \propto \nu^\alpha$ and listed in Table 3. (1) During data reduction, the MFS mode can be used with $n_{\text{terms}} \geq 2$ to model the radio spectrum in each pixel as a Taylor expansion in frequency, generating the α_{MFS} map as one of the cleaning products. (2) As the observing frequency spans from 4.25 to 8.2 GHz, the in-band spectral indices α_{inband} can be measured by cleaning two frequency bands with a bandwidth of 2 GHz respectively. These two methods are somewhat similar in that they take advantage of the spectral range of our VLA observations, but spectral indices between 4.25 and 8.2 GHz for individual sources can only be obtained by methods (1) and (2) when their flux densities $F_\nu \gtrsim 150 \mu\text{Jy}$. The advantage of method (1) is that if the object is bright enough, its entire spectral index map is available. However, in practice sometimes only the brightest pixel has an index measurement, which is therefore not very robust. The advantage of the more conventional method (2) is that we can calculate the uncertainty of spectral indices by propagating the uncertainty of flux densities.

(3) If a source is detected in both our VLA observation and in FIRST, its spectral index between 1.4 and 6.2 GHz can be measured. This is the case for

SDSSJ1550+0806 since it is above the FIRST catalog threshold. An additional five with $F_\nu \gtrsim 150 \mu\text{Jy}$ at 6.2 GHz are marginally detected in FIRST, and their spectral indices are measured using the peak flux densities in the FIRST images. There are some uncertainties in this method. First, these sources are detected at only $\sim 4\sigma$ levels in FIRST. Furthermore, CLEAN bias is known to affect FIRST flux densities, and while we correct the flux densities from FIRST by a CLEAN bias of the lesser of $250 \mu\text{Jy}$ or 40 per cent of the measured peak flux densities (White et al. 2007), it may have a poorly known dependence on the location of a source in an image as well as on the flux density of the source. SDSSJ2215–0056 is detected in the deeper 1.4 GHz radio observations of the Stripe 82 catalog (Hodge et al. 2011), and therefore its spectral index between 1.4 GHz and 6.2 GHz is available. When we calculate the spectral index for SDSSJ2215–0056, we correct it for the CLEAN bias of $35 \mu\text{Jy}$, which is not included in the Stripe 82 source catalog.

For fainter sources, we use the stacking methods to obtain average spectral indices. (4) By stacking VLA images in two frequency bands, we can measure the average spectral indices between 4.25 and 8.2 GHz. To avoid heavily weighting the brighter sources, we calculate the average spectral indices $\langle\alpha\rangle$ by normalizing the contribution of each object by its flux density at the central frequency:

$$\langle\alpha\rangle_{\text{inband}} = \frac{\log\left(\sum_i \frac{F_{i,1}}{F_{i,c}} / \sum_i \frac{F_{i,0}}{F_{i,c}}\right)}{\log(\nu_1/\nu_0)}, \quad (1)$$

where $\nu_0 = 5.1215$ GHz and $\nu_1 = 7.2635$ GHz. $F_{i,c}$ is the flux density of object i at the central frequency 6.2 GHz, while $F_{0,c}$ and $F_{1,c}$ are the flux densities at ν_0 and ν_1 respectively.

(5) By stacking the FIRST images, we can also measure the average spectral indices between 1.4 and 6.2 GHz, normalizing the contribution of each object by its flux density at 6.2 GHz:

$$\langle\alpha\rangle_{\text{outband}} = \frac{\log\left(\sum_i \frac{F_{i,6.2}}{F_{i,6.2}} / \sum_i \frac{F_{i,1.4}}{F_{i,6.2}}\right)}{\log(\nu_{6.2}/\nu_{1.4})} = \frac{\log\left(N / \sum_i \frac{F_{i,1.4}}{F_{i,6.2}}\right)}{\log(\nu_{6.2}/\nu_{1.4})}, \quad (2)$$

where $\nu_{1.4} = 1.4$ GHz and $\nu_{6.2} = 6.2$ GHz. $F_{i,1.4}$ and $F_{i,6.2}$ are the flux densities of object i at 1.4 and 6.2 GHz respectively, and N is the number of sources used in the stacking. In contrast to the flux density measurement of individual objects, for stacking we use the peak flux density of the brightest pixel, and the uncertainty of the average spectral indices is estimated by bootstrapping analysis. We apply a CLEAN bias of 40 per cent

of the peak flux density to the FIRST measurements. For methods (4) and (5), we also measure the spectral indices without flux density normalization, and the difference in the spectral indices resulting from methods with or without weights is smaller than their reported uncertainties.

3. RADIO PROPERTIES OF ERQS

3.1. Radio luminosity distribution

While the exact shape of the radio luminosity distribution continues to be under debate, objects at the bright end of the radio luminosity function are conventionally called ‘radio-loud’, and this part of the AGN population has long been associated with powerful jets (Urry & Padovani 1995). The exact dividing line between the radio-loud and the radio-quiet population is difficult to determine, and in fact may depend on the bolometric luminosity of the AGN and other properties. Traditionally, radio-to-optical ratios have been used to delineate radio-loud from radio-quiet sources, but such measures are not particularly meaningful for ERQs whose optical emission is affected by obscuration as is clear from their spectral energy distributions (Zakamska et al. 2016a; Hamann et al. 2017). Another possibility is to use forbidden emission lines which are emitted on larger scales and are less affected by obscuration (Xu et al. 1999). For the typical [O III] luminosity of ERQs of $10^{10} L_{\odot}$ (Zakamska et al. 2016a), Xu et al. (1999) would consider AGNs with $\nu L_{\nu}[5 \text{ GHz}] \gtrsim 10^{41.8} \text{ erg s}^{-1}$ radio-loud.

The flux densities used for calculating the luminosity function of ERQs are listed in Table 4. Given a median noise level of $7.6 \mu\text{Jy}$, the typical detection threshold for our observations is $4\sigma \sim 30 \mu\text{Jy}$. At this sensitivity, radio emission is detected at 6.2 GHz in 65 out of 101 sources in our VLA observations. Radio luminosities are computed using equation

$$\nu L_{\nu} = 4\pi D_L^2 (1+z)^{-1-\alpha} (\nu/\nu_{\text{obs}})^{1+\alpha} \nu_{\text{obs}} F_{\nu_{\text{obs}}}, \quad (3)$$

where D_L is the luminosity distance at redshift z . For comparison with previous studies, we k -correct to rest-frame $\nu = 6 \text{ GHz}$, with $\nu_{\text{obs}} = 6.2 \text{ GHz}$ for our VLA observations and $\nu_{\text{obs}} = 1.4 \text{ GHz}$ for objects with FIRST catalog detections. We adopt a spectral index of $\alpha = -0.7$ for the k -correction. Although the spectral indices of brighter individual sources can be measured, we use $\alpha = -0.7$ for them in order to be consistent with fainter sources in the measurements. If instead of -0.7 , α is -1.0 , then our calculations underestimate the intrinsic luminosity at 6 GHz by a factor of ~ 1.5 , or 0.18 dex.

The distribution in radio luminosity and redshift for all ERQs in our study is shown in Figure 4. Within the limited redshift range, there is no obvious dependence of radio activity on the redshift, except that the upper limits are tracking the typical detection

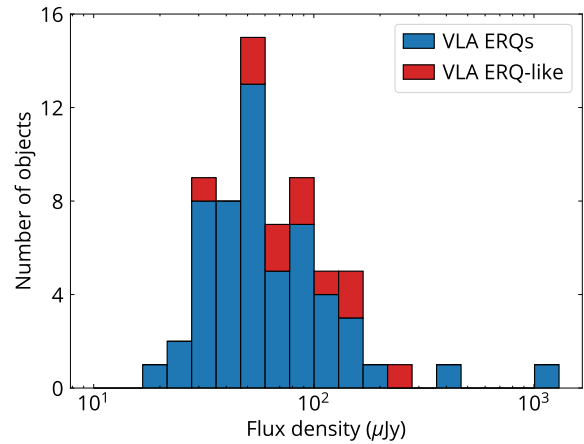


Figure 3. The distribution of flux densities observed at 6.2 GHz for ERQs detected in the VLA observations.

limit of our observations. Our dataset is nearly complete (90 per cent, including FIRST sources) down to $\nu L_{\nu}[6 \text{ GHz}] = 10^{41} \text{ erg s}^{-1}$. The radio luminosity of detected sources spans nearly three orders of magnitude, from $10^{40.5}$ to $10^{43.0} \text{ erg s}^{-1}$. The median luminosity of ERQs at 6 GHz is $1.1 \times 10^{41} \text{ erg s}^{-1}$.

In Figure 5 we present the radio luminosity distribution of ERQs in comparison with the radio luminosity distributions of several other quasar populations. Although in general ERQs and ERQ-like objects share similar properties, we exclude ERQ-like objects in this calculation to avoid potential contamination. As the number of ERQs which are not selected for the follow-up SDSS spectroscopy and therefore are not in our sample is not well-understood, we cannot compute the volume density at each radio luminosity accurately. Instead, for every bin in the logarithm of the radio luminosity, we show the fraction of objects with radio luminosities within this bin in the targeted ERQ population. In this representation, if the luminosity function is measured over the full luminosity range, then the integral under the curve should amount to 1, and differently binned luminosity functions can be directly compared to one another. In order to avoid confusion with the luminosity function defined in volume density, we use ‘luminosity distribution’ for the representation in Figure 5 in this paper. We emphasize that after we discard those objects targeted for follow-up spectroscopy only as radio sources, the selection for spectroscopy is independent of the radio properties.

The detection limit of the VLA observations is nearly complete (90 per cent) for radio luminosity above $10^{41} \text{ erg s}^{-1}$. We perform a completeness correction for the radio luminosity bin of $10^{40.8-41.0} \text{ erg s}^{-1}$ by assuming a similar radio luminosity distribution between the redshift bin $z = 2.0 - 2.4$ and the radio non-detections

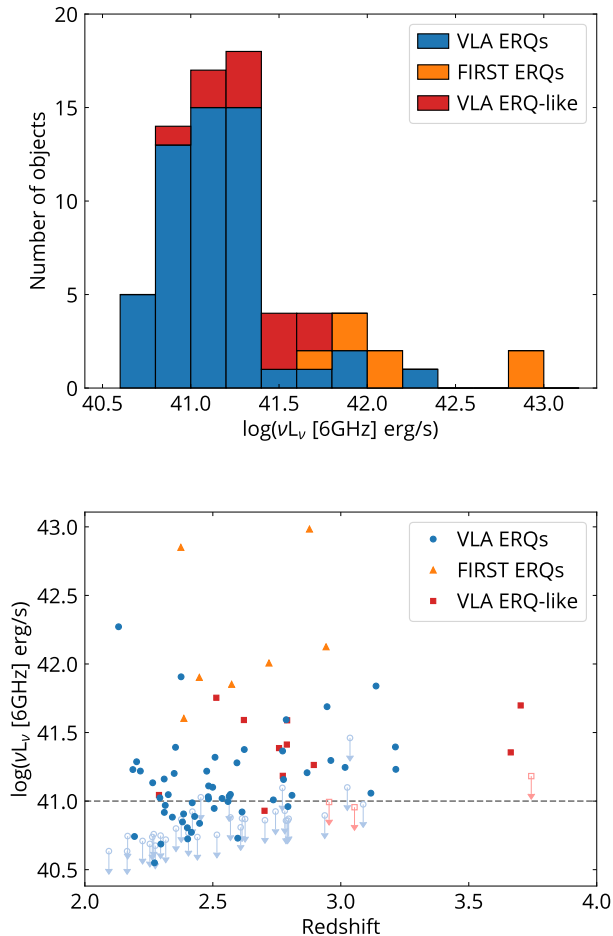


Figure 4. Top: radio luminosity distribution of radio-detected ERQs k -corrected to rest-frame 6 GHz. Bottom: radio luminosities versus redshifts. Blue dots are ERQs observed with VLA, orange triangles are ERQs detected in FIRST, and red squares are ERQ-like objects. The upper limits for non-detections are set to 4σ , where σ is the root-mean-square noise in their fields. The dashed line at $10^{41} \text{ erg s}^{-1}$ indicates the luminosity above which most (90 per cent) objects are detected over the entire redshift range.

with upper limits $> 10^{40.8} \text{ erg s}^{-1}$. Specifically, out of 32 sources in the redshift bin $z = 2.0 - 2.4$, 11 are detected above $10^{41} \text{ erg s}^{-1}$, 3 detected in $10^{40.9-41} \text{ erg s}^{-1}$, and 3 in $10^{40.8-40.9} \text{ erg s}^{-1}$. We use these detection counts to determine the probabilities of detection in the radio luminosity bin $10^{40.8-41.0} \text{ erg s}^{-1}$ for the non-detections in the entire redshift range: 5 non-detections with upper limits higher than $10^{41} \text{ erg s}^{-1}$, 4 with upper limits in $10^{40.9-41.0} \text{ erg s}^{-1}$, and 10 with upper limits in $10^{40.8-40.9} \text{ erg s}^{-1}$. This gives a completeness correction of additional four counts in the bin of $10^{40.8-41.0} \text{ erg s}^{-1}$. There are already 13 detections in this luminosity bin and thus this completeness correction and its uncertainty do not change the overall shape of the ERQ radio luminosity distribution. Error bars for the ERQ lumi-

nosity distribution are estimated using bootstrap analysis.

Out of our 101 objects, 36 sources are not detected in the VLA observations. To estimate the mean flux density for non-detected objects, we exclude 5 fields where noise levels are $> 10 \mu\text{Jy beam}^{-1}$ and stack the remaining 31 fields containing non-detections. The stack reveals a detection with the mean and median flux densities of $13.8 \pm 1.8 \mu\text{Jy}$ and $14.9 \pm 2.5 \mu\text{Jy}$ respectively, where the uncertainty is estimated by bootstrap analysis. At their median redshift $z = 2.57$, the median flux density corresponds to a radio luminosity at 6 GHz of $3.3 \times 10^{40} \text{ erg s}^{-1}$. This enables us to place the lowest radio luminosity point (red horizontal segment) in Figure 5.

The method to estimate the radio luminosity distribution for the radio non-detections from Zakamska & Greene (2014) in Figure 5 is different from that used for ERQs. In the sample of Zakamska & Greene (2014), all 7 FIRST non-detections located in Stripe 82 are detected in the deeper survey (Hodge et al. 2011) with flux densities between 0.4 and 0.7 mJy, about 2 times fainter than the detection limits of FIRST. Based on this, the radio luminosity distribution for the sample of Zakamska & Greene (2014) is derived by considering the flux densities of non-detections to be 1, 2, and 10 times fainter than their upper limits. In each case, error bars are estimated using bootstrap analysis, and the error bars in Figure 5 show the largest ones among these three cases. This calculation results in larger uncertainties when the radio luminosity is smaller than $10^{40.5} \text{ erg s}^{-1}$, while those bins above this luminosity are well constrained by the detections. The FIRST stacking of these non-detections has a median of $301 \pm 24 \mu\text{Jy}$, without a correction for the CLEAN bias. After the CLEAN bias correction, the median radio luminosity is $4.6 \times 10^{39} \text{ erg s}^{-1}$, consistent with the radio distribution of Zakamska & Greene (2014) in Figure 5.

3.2. Morphologies and spectral indices

Typically, in radio-loud AGNs flat spectral indices ($\alpha > -0.5$) are due to relativistic boosting of self-absorbed synchrotron spectra arising in a compact $\lesssim 1$ pc core, whereas steep spectral indices ($\alpha < -0.5$) are due to unboosted radio emission arising on larger scales (Blandford & Königl 1979; Orr & Browne 1982). Spectral indices of radio-quiet AGNs are still not well known due to the lack of a sensitive all-sky radio survey at a different frequency from FIRST.

Spectral indices measured by methods described in Section 2.4 are listed in Table 3. Our inband spectral indices correspond to rest-frame frequencies $\sim 15 - 30$ GHz, and our outband spectral indices correspond to rest-frame $\sim 5 - 20$ GHz. Because the observed radio

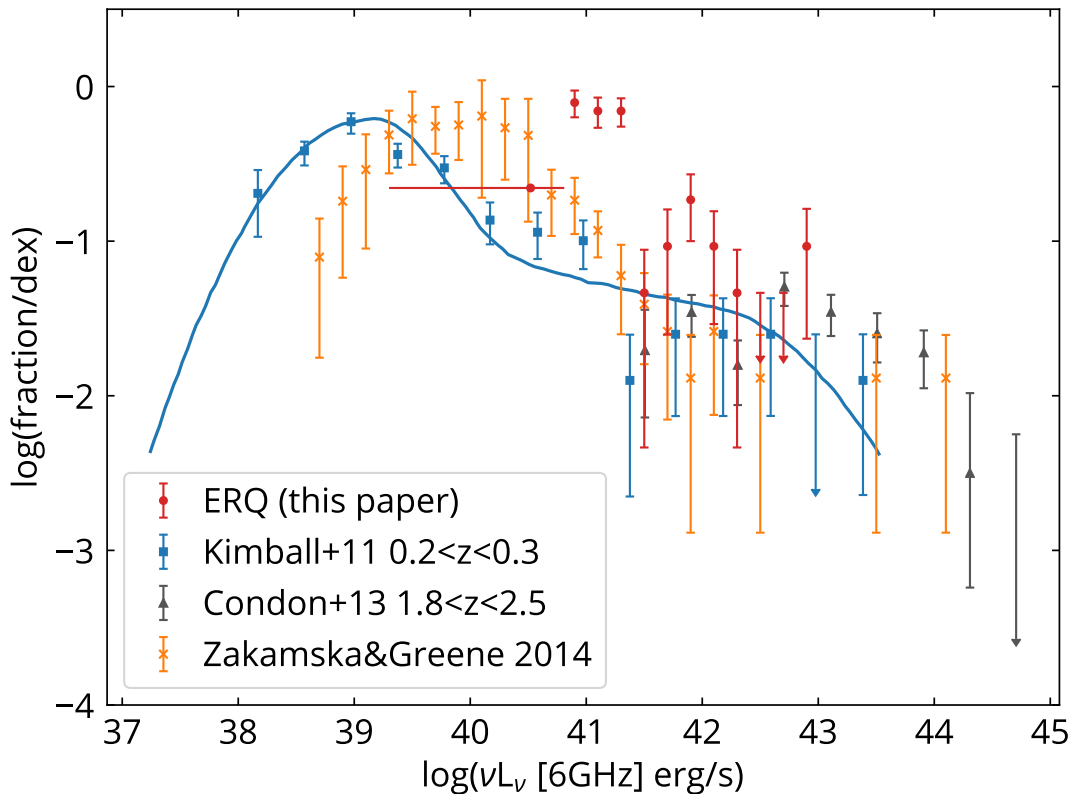


Figure 5. The distribution of radio luminosity at rest-frame 6 GHz, presented in the fraction of overall parent population per logarithmic bin. The red dots represent ERQs in this paper, and the red horizontal segment is the estimated radio luminosity for 36 non-detections, where the horizontal range indicates the standard deviation of the overall radio luminosity distribution for non-detections, estimated by bootstrap analysis. For comparison, the blue squares are for the low-redshift AGN sample in [Kimball et al. \(2011\)](#), the orange crosses are for $z < 0.8$ type 2 quasars in [Zakamska & Greene \(2014\)](#) and the grey triangles are for high-redshift type 1 quasars in [Condon et al. \(2013\)](#). The error bars of the sample from [Zakamska & Greene \(2014\)](#) are estimated by considering the flux densities of radio non-detections to be 1, 2, and 10 times fainter than their upper limits, resulting in larger uncertainty. The radio-quiet bulk of the high-redshift type 1 quasar population is not detected by [Condon et al. \(2013\)](#) and is therefore not shown. Compared to other AGN samples, the radio luminosities of ERQs are concentrated around a much higher median luminosity $1.1 \times 10^{41} \text{ erg s}^{-1}$.

spectra are steep, free-free emission, which has a spectral index of -0.1 , cannot dominate the radio emission of ERQs at these frequencies. In order to get measured $\alpha_{\text{inband}} = -1.0$, the fraction of free-free emission is limited to ~ 40 per cent at rest-frame ~ 20 GHz, assuming that the underlying synchrotron spectrum cannot be steeper than $\alpha = -1.5$. This fraction should be considered as a conservative upper limit because we do not see significantly flatter α_{inband} compared to α_{outband} , which is expected if free-free emission dominates at higher frequencies. At face value, this upper limit on the free-free emission suggests that the star formation rates in ERQ hosts must be limited to $\sim 2000 M_{\odot} \text{ yr}^{-1}$ ([Murphy et al. 2012](#)). This conversion is uncertain because the existing scalings between free-free emission and star formation have not been calibrated in this radio luminosity regime.

ERQ SDSSJ1117+4623 is the brightest object (1.25 mJy at 6.2 GHz , or $\nu L_{\nu}[6\text{GHz}] = 1.9 \times 10^{42} \text{ erg s}^{-1}$) in our VLA observations. It is also marginally detected in FIRST with the brightest pixel having an intensity of $0.73 \text{ mJy beam}^{-1}$, though it is not bright enough to be listed in the FIRST catalog. Its spectral index between rest-frame 12 and 25 GHz is $+0.29 \pm 0.15$ (MFS mode) or alternatively $+0.37 \pm 0.09$ (two-band imaging), while the spectral index between rest-frame 4 and 19 GHz is $+0.17 \pm 0.10$, corrected for the CLEAN bias of FIRST. These measurements are consistent with one another within the uncertainties. Among the sources with measurable spectral indices, SDSSJ1117+4623 is the only one with a flat spectral index of $\alpha > -0.5$. Interestingly, while the main source itself is not spatially resolved, there is a marginally resolved faint ra-

dio source with a peak intensity of $55 \mu\text{Jy beam}^{-1}$ and an integrated flux density of $90 \mu\text{Jy}$ to the south-east of SDSSJ1117+4623 at a projected distance of 80 kpc (Figure 2). This object lacks an SDSS counterpart, and we hypothesize that SDSSJ1117+4623 consists of a flat-spectrum core and a lobe with a hotspot. Therefore, the radio emission from this source may be due to a jet. However, it is still possible that the extended radio source is from an unrelated source. For example, dust strongly attenuates UV and optical light but does not affect radio wavelengths, resulting in the non-detection in SDSS.

Aside from SDSSJ1117+4623, all other sources with individually measured spectral indices have steep radio spectra with α ranging from -1.8 to -0.7 and they are all point-like – the fitted 2D elliptical shapes we use for measuring flux densities are consistent with the theoretical PSF provided by CASA. The stacking analysis of fainter sources without individual indices also yields steep spectra. The brighter flux density bin ($80 - 150 \mu\text{Jy}$) shows an average spectrum with $\alpha = -1.08 \pm 0.25$, and the fainter flux density bin ($30 - 80 \mu\text{Jy}$) shows an even steeper average spectrum with $\alpha = -1.35 \pm 0.34$.

The stacks reveal extended emission between 2 and 3 arcsec from the center of the synthesized beam, inconsistent with the expectations from the Gaussian beam shape and with an average intensity excess of $\sim 2 \mu\text{Jy beam}^{-1}$. Because the flux density of the extended emission is sensitive to the cleaning threshold, we suspect this is a cleaning artifact, with residual PSF below the cleaning threshold.

4. DISCUSSION

4.1. Summary of observed ERQ properties

In the previous section, we find that, as a population, ERQs have the following radio properties:

- At rest-frame 6 GHz, 9 ERQs (~ 8 per cent of the population) have radio luminosities νL_ν in excess of $10^{41.8} \text{ erg s}^{-1}$, the nominal ‘radio-loud’ definition we adopt for this population based on the [O III] luminosity ($\log L_{5\text{GHz}} = 24 \text{ W Hz}^{-1} \text{ Sr}^{-1}$ in Xu et al. 1999). This fraction is qualitatively similar to the radio-loud fractions of other quasar sub-populations, though it depends sensitively on the exact definition. Since ERQs are candidate high-redshift obscured quasars, we compare their radio-loud fraction to that of low-redshift type 2 quasars and find that the radio-loud fraction is similar (~ 8 per cent; Zakamska et al. 2004) when the [O III]-based radio-loudness definition is adopted.
- The median 6 GHz radio luminosity is $1.1 \times 10^{41} \text{ erg s}^{-1}$, with ~ 78 per cent of the pop-

ulation with luminosities between $10^{40.0}$ and $10^{42.0} \text{ erg s}^{-1}$. This median radio luminosity is ~ 1.5 dex higher than the low-redshift sample from Zakamska & Greene (2014), and ~ 0.5 dex higher than the sample from Condon et al. (2013).

- We find no sources extended on $\gtrsim 10$ kpc scales except for one powerful source SDSSJ1117+4623 on the radio-loud end of the distribution, which can be explained as a jet core+lobe system.
- With the exception of the same core+lobe system which has a flat spectrum core, ERQs have steep radio spectra with $\langle \alpha \rangle$ between -1.0 and -1.3 depending on the measurement method and a standard deviation within the population of 0.3.

As ERQs were selected by their high mid-infrared-to-optical ratios, it is not surprising that their spectral energy distributions steeply rise from optical to infrared wavelengths (Zakamska et al. 2016a; Hamann et al. 2017). Dust obscuration with A_V of a few to 10 mag can account for the shape of the near-infrared spectral energy distribution, but not for the rest-frame ultra-violet continuum which is too strong and too blue to be directly visible reddened light from the quasar (Hamann et al. 2017). Alexandroff et al. (2017) demonstrate that the rest-frame ultraviolet continuum is highly polarized and is therefore largely due to scattered light, as expected in the classical geometric unification model of AGNs (Antonucci 1993) and as seen in low-redshift powerful type 2 quasars (Zakamska et al. 2006; Greene et al. 2012; Obied et al. 2016). Goulding et al. in prep. find that ERQs are high-luminosity ($L_X \gtrsim 10^{45} \text{ erg s}^{-1}$), strongly obscured ($N_H \simeq 10^{24} \text{ cm}^{-2}$) X-ray emitters. In summary, ERQs show multi-wavelength properties consistent with a luminous, obscured quasar population, where the powerful infrared emission is produced by warm dust near the quasar. In particular, the spectral energy distribution is inconsistent with BL Lac-type synchrotron-dominated spectra (Fossati et al. 1998) which have flatter radio indices with no strong variations in the spectral energy distribution as a function of wavelength analogous to the steep rise seen in ERQs toward infrared wavelengths, so we do not consider this possibility further.

Follow-up near-infrared spectroscopy reveals outflows of ionized gas as traced by the [O III] emission with unprecedented kinematics (Zakamska et al. 2016a, Perrotta et al. in prep). The ERQs’ infrared luminosities (obtained from the apparent $W3$ and $W4$ fluxes) at rest-frame $5 \mu\text{m}$ range from $10^{46-47} \text{ erg s}^{-1}$ (Zakamska et al. 2016a; Hamann et al. 2017), with a median of $10^{46.4} \text{ erg s}^{-1}$ for the objects in our radio sample. To estimate the bolometric luminosity, we use a bolo-

metric correction factor of 8 (Richards et al. 2006) to arrive at the median bolometric luminosity of $L_{\text{bol}} = 10^{47.3} \text{ erg s}^{-1}$. As the Eddington mass for a luminosity of $10^{47} \text{ erg s}^{-1}$ is $\sim 10^9 M_{\odot}$, ERQs might be accreting at near- or even super-Eddington levels, which may explain their unusually strong outflow activity. Given this context for multi-wavelength properties of ERQs, in the following sections we discuss the origin of the radio emission from ERQs.

4.2. *Is radio emission from ERQs due to star formation?*

Radio synchrotron emission is a known by-product of star formation, as supernova explosions shock the interstellar medium, enriching the galaxy with relativistic particles. This process results in a strong correlation between far-infrared luminosities and radio luminosities in star-forming galaxies (Helou et al. 1985). The median ERQ radio luminosity of $\nu L_{\nu}[6 \text{ GHz}] = 1.1 \times 10^{41} \text{ erg s}^{-1}$ would require a star formation rate of $2700 M_{\odot} \text{ yr}^{-1}$ (Bell 2003). This is an extremely high value, but it does not contradict the observed infrared fluxes from *WISE*. By scaling the templates of spectral energy distributions of star-forming galaxies (Rieke et al. 2009) to these star formation rates, we find that the *W4* fluxes expected from star formation of this level are 4 magnitudes fainter than observed, indicating that the *WISE* fluxes of ERQs are dominated by quasar activity, not star formation.

Such values of star formation are not found in the local Universe, and they are at the upper limit of values found in the most luminous submillimeter galaxies at ERQ redshifts (Blain et al. 2002; Chapman et al. 2005). Is it possible that ERQ host galaxies support these levels of star formation required to explain the observed radio emission? While there are not yet far-infrared measurements of star formation available for ERQs, some authors have argued that the star formation in a closely related population – hot dust obscured galaxies (HotDOGs; Fan et al. 2016; Farrah et al. 2017) – can contribute 10–20 per cent of the bolometric luminosity, which at $L_{\text{bol}} = 10^{47.3} \text{ erg s}^{-1}$ would translate into 900–1800 $M_{\odot} \text{ yr}^{-1}$ (Bell 2003). These are also extremely high values, but they are smaller than is required to power the median radio luminosity in our sample. Therefore, the top 50 per cent of the radio luminosities of the radio-quiet ERQs ($10^{41} - 10^{42} \text{ erg s}^{-1}$) are hard to reconcile with star formation.

Another puzzle is the steep radio spectra of ERQs. In local starburst galaxies, the radio spectral indices at $\sim \text{GHz}$ frequencies are expected to be -0.7 , flattening both at higher frequencies (10–100 GHz) where free-free emission contributes (Murphy et al. 2011, 2012) and at lower frequencies where in compact starbursts self-

absorption effects become important (Murphy 2013). In contrast, the mean spectral index of ERQs is -1.0 with one source showing $\alpha = -1.8$, significantly different from the expected values of starburst galaxies. Ibar et al. (2010) study the radio-identified submillimeter galaxies at $z \sim 2$ and measure a mean spectral index between 610 MHz and 1.4 GHz of -0.75 ± 0.06 , indistinguishable from those of local starburst galaxies and appreciably higher than those of ERQs. A comparison of ERQs with this population suggests that the radio emission in ERQs is not powered by star formation.

In starburst galaxies, inverse Compton scattering might accelerate cooling and steepen the synchrotron spectra (Seaquist & Odegard 1991). However, this process would also suppress radio emission, making it even more difficult to reproduce the observed radio emission with star formation in ERQs. Thus on the balance of available data we find it unlikely that star formation dominates the radio luminosity of ERQs. The required star formation rates are too high on the upper end of the radio-quiet subset of ERQs ($\nu L_{\nu} \lesssim 10^{42} \text{ erg s}^{-1}$), and the spectral indices are steeper than those that are found both in local starbursts and in high-redshift submillimeter galaxies.

4.3. *Shape of the radio luminosity distribution*

In Figure 5, we compare the radio luminosity distribution of ERQs with three other datasets: nearby type 1 quasars (Kimball et al. 2011), intermediate redshift type 2 quasars (Reyes et al. 2008; Zakamska & Greene 2014) and high-redshift type 1 quasars (Condon et al. 2013). All of the observations are based on optically selected sample, and they have been corrected to rest-frame 6 GHz here. The most complete coverage of the radio luminosity function was achieved by Kimball et al. (2011) who detect 173 out of 179 quasars in their sample at $0.2 < z < 0.3$ and fit a two-population model to their observed radio luminosity function. By comparing their data to the radio luminosity functions of star-forming galaxies and AGNs, they suggest that the peak centered at $10^{39} \text{ erg s}^{-1}$ is due to star formation, whereas AGNs dominate radio output at brighter luminosities. The star formation rate of $25 M_{\odot} \text{ yr}^{-1}$ required to explain the median radio luminosity is high but not unreasonable.

A similar argument was put forward by Condon et al. (2013) who present the radio luminosity function of 2471 type 1 quasars at $1.8 < z < 2.5$. Only 8 per cent – the radio-loud end of the population – are detected at $F_{\nu} > 2.4 \text{ mJy}$ by the National Radio Astronomy Observatory VLA Sky Survey (NVSS; Condon et al. 1998), and those are the objects shown with data points in Figure 5. By analyzing the statistics of the radio maps of undetected sources, these authors suggest that

there is a peak of the luminosity function at faint luminosities with an estimated median radio luminosity $\nu L_\nu = 10^{40.4} \text{ erg s}^{-1}$, which we have translated to rest-frame 6 GHz for direct comparison with our data assuming $\alpha = -0.7$. By stacking radio data, [White et al. \(2007\)](#) find similar mean radio luminosities for the most optically luminous quasars in their sample. [Condon et al. \(2013\)](#) argue that this peak may be due to powerful star formation in the quasar hosts at the level of $\sim 500 \text{ M}_\odot \text{ yr}^{-1}$, though no independent star formation measures for this population are available to probe this hypothesis.

We also present the radio luminosity function of $z < 0.8$ type 2 quasars from the sample of [Zakamska & Greene \(2014\)](#), where to avoid biasing our measurements to high radio luminosities we have excluded all objects targeted for follow-up SDSS spectroscopy only due to their radio emission. The median radio luminosity of this sample, translated again to rest-frame 6 GHz, is $10^{40.2} \text{ erg s}^{-1}$, which would correspond to a star formation rate of $\sim 300 \text{ M}_\odot \text{ yr}^{-1}$ ([Bell 2003](#)). However, for this sample several multi-wavelength measures of star formation are available and are strongly inconsistent with the star formation rates implied by the observed radio luminosity, so that only ~ 10 per cent of the observed radio luminosity can be due to star formation ([Zakamska et al. 2016b](#)). In other words, another mechanism is required to explain the radio emission of powerful type 2 quasars. As these objects are unresolved at 5 arcsec ($\sim 30 \text{ kpc}$) scales in the FIRST survey, there is no evidence that their radio emission is due to large-scale jets.

To summarize, even for a narrow range of bolometric luminosities or optical properties of AGNs, the radio luminosity distribution can span over six orders of magnitude. The radio luminosity cannot fall below that associated with star formation in the host galaxy, and this star formation component can dominate the lower end of the radio luminosity function ([Kimball et al. 2011](#); [Rosario et al. 2013](#)). On the ‘radio-loud’ end, we have a population that has long been associated with powerful jets ([Urry & Padovani 1995](#)). The nature of the radio emission in the intermediate radio luminosity $10^{39} - 10^{42} \text{ erg s}^{-1}$ range is surprisingly ambiguous, and this is exactly the regime in which the radio luminosity distribution of ERQs peaks. Furthermore, we find that the peak of the luminosity distribution of ERQs occurs at appreciably higher radio luminosities than the peaks for the comparison samples, while ERQs still remain predominantly radio-quiet.

Various possible mechanisms have been discussed to explain the radio output of AGNs in this intermediate luminosity range. One possibility is coronal emission around the accretion disks ([Laor & Behar 2008](#); [Ra-](#)

[ginski & Laor 2016](#)). Because this emission arises on scales $\lesssim 10^5$ Schwarzschild radii, it is expected to be optically thick to synchrotron self-absorption at the frequencies of our observations and therefore have flat spectra ($\alpha = 0$). As ERQs have steep radio spectra, we rule out this mechanism as the dominant origin of their radio emission.

In [Figure 5](#), the radio luminosity distributions of ERQs and of quasars from [Kimball et al. \(2011\)](#) and [Condon et al. \(2013\)](#) show a local minimum at $\sim 10^{41.4} \text{ erg s}^{-1}$. Interestingly, this minimum appears in the radio luminosity functions of quasars of widely different bolometric luminosities, which is in contradiction with a luminosity-dependent dearth of radio sources seen by [Xu et al. \(1999\)](#). A local minimum at $\sim 10^{41.4} \text{ erg s}^{-1}$ in the luminosity function suggests that different mechanisms might be responsible for the radio emission below and above this value.

We now proceed to comparing the features in the luminosity distributions shown in [Figure 5](#) to the traditional divides between radio-loud and radio-quiet objects. Because ERQs are obscured at optical wavelengths, we use the rest-frame infrared luminosity at $5 \mu\text{m}$ as an indicator of bolometric luminosity ([Goulding et al., submitted](#)). As a comparison sample, we use type 1 quasars in a narrow redshift range $0.5 < z < 0.7$ from DR12Q ([Pâris et al. 2017](#)) so as to avoid introducing an artificial correlation in the infrared versus radio luminosity space. The infrared luminosity at rest-frame $5 \mu\text{m}$ is obtained by power-law interpolating between *WISE* fluxes, if detected with a signal-to-noise ratio above 3. Sources targeted for follow-up SDSS spectroscopy only because of their radio emission are excluded, and the radio luminosity is corrected to rest-frame 6 GHz assuming $\alpha = -0.7$. The FIRST-matched sources constitute 4 per cent of the *WISE*-detected DR12Q sample in $0.5 < z < 0.7$, which is a typical FIRST-detection rate in SDSS quasars and is smaller compared to that of more luminous quasars like [Zakamska & Greene \(2014\)](#).

The FIRST flux densities of many quasars in DR12Q are underestimated because the radio emission of lobes is not taken into account. To improve the radio measurement, we cross-match the sample with a catalog of Fanaroff-Riley type II (FR II) sources in FIRST ([van Velzen et al. 2015](#)), and sum up the flux densities from cores and lobes. Changing the assumed spectral index from -0.7 to -0.3 would increase the calculated luminosities by 0.17 dex. Because the automated search for FR II sources is biased to brighter sources, it might result in an artificial separation around the radio luminosity limit for the automated search. To ensure that it is not the case for the separation seen in [Figure 6](#), we visually inspect the FIRST cutout images and mark those potential jets missed in the FR II catalog. Even if

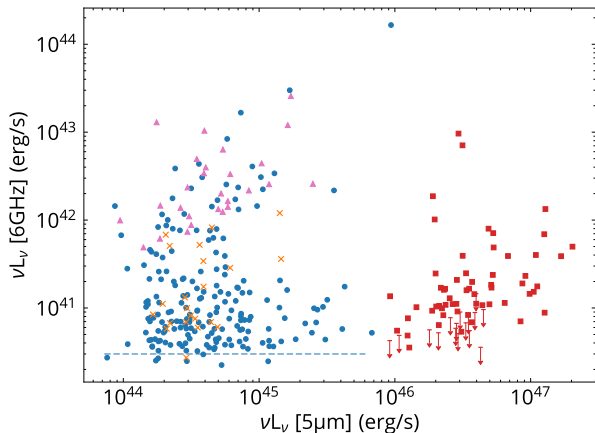


Figure 6. Radio luminosity at 6 GHz versus infrared luminosity at $5 \mu\text{m}$. The red squares represent ERQs, including ERQ-like objects and those detected in FIRST. Other symbols are quasars with redshifts $0.5 < z < 0.7$ from DR12Q (Pâris et al. 2017). The blue points adopt the radio flux densities by cross-matching with FIRST, while the pink triangles use the ones from van Velzen et al. (2015) to account for the emission from lobes. We visually inspect all sources, and use orange crosses to indicate jet candidates whose radio luminosities may be underestimated. The dashed line is the radio luminosity above which the low-redshift sample is complete over its redshift range.

their radio luminosities are underestimated, their lower infrared luminosities show that the separation in Figure 6 is not artificial.

The local minimum in the ERQ radio distribution at $10^{41.4} \text{ erg s}^{-1}$ is consistent with the separation between the radio-loud and radio-quiet population among type 1 quasars. Therefore, we conclude that ERQs are a predominantly radio-quiet population. The radio luminosity distribution of type 1 quasars with FR II morphology is markedly different from their overall luminosity distribution and is heavily biased toward higher radio luminosities. Therefore, we speculate that the traditional boundary separating radio-loud versus radio-quiet objects (which appears to happen at $10^{41.4} \text{ erg s}^{-1}$ in both populations in Figure 6) corresponds to the transition from the jet-dominated population to other mechanisms. Further measurements of radio luminosity functions, of radio morphologies and of radio spectral indices for other AGN populations around this critical luminosity will clarify the nature of this feature.

4.4. Radio emission and ionized gas kinematics

In the previous sections, we argued against star formation and ruled out large-scale jets and coronal emission as the origin of the radio emission of radio-quiet ERQs. In the following sections, we consider the remaining two mechanisms – shocks caused by wide-angle quasar winds (Zakamska & Greene 2014; Nims et al. 2015) and com-

compact jets launched by central supermassive black holes (Falcke et al. 2004; Leipski et al. 2006).

ERQs are extremely powerful quasars, which likely accrete at near-Eddington or even super-Eddington rates. On nuclear scales, such objects can produce powerful outflows via a variety of mechanisms. Radiatively driven winds in which photons are absorbed by partially ionized gas (Murray et al. 1995; Proga et al. 2000; Proga & Kallman 2004) are a strong possibility given that ERQs show signatures of absorption-line troughs in their SDSS spectra (Hamann et al. 2017). Winds launched by radiation pressure on dust (Murray et al. 2005; Thompson et al. 2015) have been recently suggested specifically to explain properties of powerful red quasars at high redshifts (Ishibashi et al. 2017). Mechanisms that involve magnetic fields are also possible (Königl & Kartje 1994; Everett 2005).

As these winds propagate into the surrounding interstellar medium and interact with it, the resulting shocks can produce relativistic particles which in turn yield synchrotron emission (Stoche et al. 1992). Indeed, there are indications that radio emission with luminosity $10^{39} - 10^{42} \text{ erg s}^{-1}$ is related to outflow activity on galactic scales (Mullaney et al. 2013; Zakamska & Greene 2014). Specifically, Zakamska & Greene (2014) use low-redshift type 2 quasars to find a correlation between radio luminosity and the velocity width of the [O III] emission line (Heckman et al. 1981), a forbidden transition which arises in regions with density below the critical ($8 \times 10^5 \text{ cm}^{-3}$) and is now seen by multiple groups in outflow on several kpc scales in integral field unit observations (Liu et al. 2013; Carniani et al. 2015; Rupke et al. 2017).

In this section, we test the hypothesis that the radio emission in ERQs is produced in a way similar to that in type 2 quasars. To this end, we check whether ERQs follow the correlation established for low-redshift type 2 quasars (Zakamska & Greene 2014). For these objects, the relationship between radio luminosity and w_{90} , the width (in km s^{-1}) of the 90 per cent of the [O III] line profile power, is shown with blue dots in Figure 7 where again we have removed all objects targeted for SDSS spectroscopy only because of their radio emission. For wide-angle outflows, w_{90} is a good proxy for outflow velocity and is roughly two times higher than the median radial velocity of outflowing material. Zakamska & Greene (2014) suggest that the relationship is well-fit by $L_{\text{radio}} \propto w_{90}^2$, implying a linear correlation between the radio power and the kinetic energy of the outflow, which may be naturally expected if a fixed fraction of the outflow energy is transferred into relativistic particles. With the fixed quadratic slope and with over half of the sample detected, the median relationship of radio-quiet

sources is well determined:

$$\begin{aligned} \log(\nu L_\nu[1.4 \text{ GHz}], \text{ erg s}^{-1}) \\ = 2 \times \log(w_{90}, \text{ km s}^{-1}) + 33.80, \end{aligned} \quad (4)$$

and the shaded region shows the root-mean-square spread of 0.56 dex, which encompasses 65 per cent (128/196) of the detected radio-quiet type 2 quasars. Including radio-loud type 2 quasars (with radio luminosities $> 10^{41.6} \text{ erg s}^{-1}$ at 1.4 GHz based on Xu et al. 1999) has little effect on the fitting; it changes the intercept from 33.80 to 33.84 and results in a larger scatter (0.69 dex).

We have been conducting near-infrared spectroscopic follow-up of the ERQs (Zakamska et al. 2016a; Perrotta et al. in prep), and, as of this writing, 27 [O III] measurements are available and are shown in Figure 7. As is pointed out by Zakamska et al. (2016a), ERQs show unprecedented outflow velocities as traced by the [O III] emission and lie on the extreme end of the w_{90} distribution. However, it is currently not known which, if any, of the ERQ properties and its selection criteria are particularly predictive of the presence of the high-velocity [O III] outflows. While values of w_{90} in excess of 3000 km s^{-1} are almost never seen in low-redshift samples, ERQs show an excellent agreement with the extrapolation of the correlation from Zakamska & Greene (2014): all radio-quiet radio-detected ERQs lie in the shaded region, with a root-mean-square scatter of 0.24 dex. While the dynamic range in w_{90} probed by ERQs is too small to see the correlation within this population alone, the excellent agreement with the correlation at low redshifts strongly suggests a physical connection between radio emission and ionized gas kinematics.

4.5. Winds as the origin of the radio emission in ERQs

Multiple authors have discussed radio emission associated with particles accelerated on shocks which propagate through the host galaxy as a result of quasar-driven winds (e.g., Jiang et al. 2010; Nims et al. 2015). For quasar bolometric luminosities $10^{45} - 10^{46} \text{ erg s}^{-1}$, the radio luminosities predicted by these models are $\sim 10^{40} \text{ erg s}^{-1}$, in the range suggested by the observations of type 2 quasars. Scaling this up to ERQ luminosities suggests that this process might naturally explain the radio luminosities of ERQs. Jiang et al. (2010) also point out that the spectral index at 5 GHz can steepen to $\alpha < -0.8$ in $< 0.3 \text{ Myr}$ with the observable synchrotron lifetime of $\sim 5 \text{ Myr}$ due to radiative and adiabatic cooling, which may explain the steep radio spectra in ERQs.

The existing models are idealized, with a spherically symmetric, smooth distribution of the interstellar medium. To further explore the wind hypothesis, we adopt a phenomenological approach to estimating a

plausible radio luminosity resulting from quasar-driven winds, following Zakamska & Greene (2014). We assume that ERQs are capable of converting a fraction η of their bolometric luminosity into the kinetic energy of the outflow. Then we assume that the fraction of energy that a strong shock can transfer to synchrotron-emitting particles is independent of the nature of that shock (Spitkovsky 2008) and take a lesson from starburst galaxies, in which 5.6×10^{-5} of the available mechanical energy supplied by stellar outflows and supernovae is transferred to the 6 GHz radio luminosity (Leitherer et al. 1999; Bell 2003; Zakamska & Greene 2014). This conversion factor is the heart of the strong correlation between the far-infrared emission (which measures star formation rate) and the radio emission in star-forming galaxies (Helou et al. 1985), but now we are considering the kinetic energy of the outflow powered by the quasar instead.

The median bolometric luminosity of ERQs is $10^{47.3} \text{ erg s}^{-1}$, so that the median kinetic power of their outflows is $\eta 10^{47.3} \text{ erg s}^{-1}$. Applying the conversion factor from kinetic power to radio luminosity, we expect a median radio luminosity of $1.1\eta \times 10^{43} \text{ erg s}^{-1}$. The observed median radio luminosity of ERQs is $1.1 \times 10^{41} \text{ erg s}^{-1}$ would then require that $\eta = 1$ per cent of the bolometric luminosity be converted to the kinetic power of winds. This value is in the range of the bolometric-to-kinetic conversion efficiency of quasar-driven outflows deduced from ionized gas (Liu et al. 2013; Rupke et al. 2017; Sun et al. 2017) and molecular gas (Fiore et al. 2017) phases, and is somewhat smaller than the bolometric-to-thermal conversion inferred from the Sunyaev-Zeldovich effect (> 10 per cent from Crichton et al. 2016). If the observed radio emission is suppressed by rapid cooling (Jiang et al. 2010) or inverse Compton losses (Nims et al. 2015), then the value of η we infer by applying the efficiency of radio emission taken from star-forming galaxies should be regarded as a lower limit.

To summarize, the wind scenario is consistent with the observed radio properties of ERQs. The radio luminosities of ERQs concentrate around the median luminosity of $1.1 \times 10^{41} \text{ erg s}^{-1}$, an intermediate regime where radio luminosities are too high to be explained by star formation but too low to be characteristic of classical powerful jets. The correlation between [O III] line width and radio emission implies a connection between the wind and the observed synchrotron radiation, and we suggest that the synchrotron-emitting particles are accelerated as the wind shocks the interstellar material of the host galaxy. The observed radio emission can be explained by winds if ~ 1 per cent of the bolometric luminosity is converted to the kinetic energy of wind, which is consistent with other available estimates. The

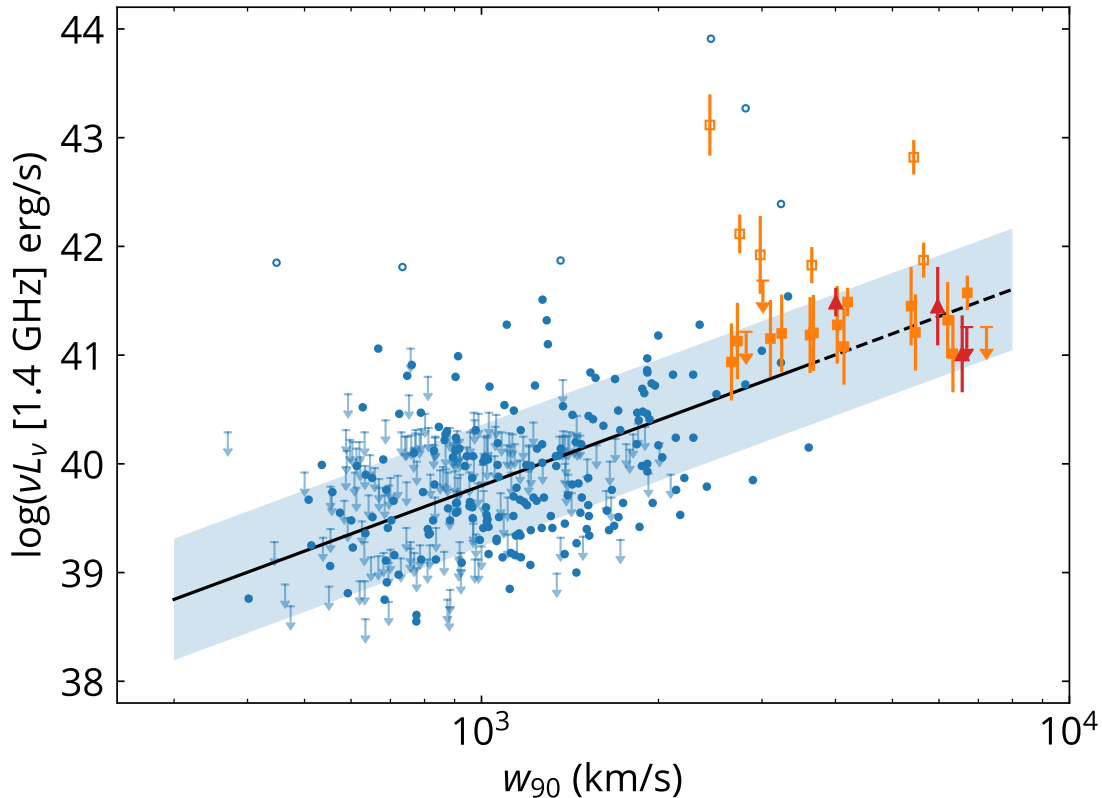


Figure 7. Radio luminosity at 1.4 GHz versus the velocity width w_{90} of the [O III] emission for radio-quiet sample. The blue dots are from the low-redshift $z < 0.8$ type 2 quasars (Zakamska & Greene 2014), with radio luminosity upper limits of $\sim 5\sigma$ from FIRST and NVSS. The red triangles (Zakamska et al. 2016a) and orange squares (Perrotta et al. in prep) represent ERQs with existing [O III] observations. Their redshifts range from $z = 2.36 - 2.94$ and the upper limits of radio luminosity are 4σ . For ERQs without individual spectral indices, we use $\alpha = -1$ with error bars obtained by assuming $\alpha = -0.7$ and $\alpha = -1.3$. The black line is the quadratic fit derived based exclusively on the low-redshift radio-quiet sample (blue solid dots), and the shaded region represents the root-mean-square scatter. The dashed extension is to show that ERQs are not used for fitting. ERQs are located at the extreme end of both [O III] kinematics and radio luminosity and closely follow the correlation established for low-redshift type 2 quasars. Open symbols designate candidate radio-loud sources.

steepness of the observed radio spectra is puzzling, but may be explained by rapid cooling, which is supported by theoretical work (Jiang et al. 2010). The unresolved radio morphology at ~ 10 kpc scales is consistent with winds confined to their host galaxies; this emission may be resolvable in higher-resolution observations (Harrison et al. 2015; Alexandroff et al. 2016).

4.6. Compact jets as the origin of ERQ radio emission

Since all ERQs except for one are unresolved on scales ~ 10 kpc, large-scale radio jets do not dominate the radio emission of ERQs. We can also rule out core-dominated sub-parsec jets which, like radio coronae, would appear with flat spectra due to synchrotron self-absorption. However, there is a known class of jet-dominated objects – compact steep-spectrum sources – which are young enough to be confined to the host galaxy by interactions with the galactic gas, but have

grown to sizes above the synchrotron self-absorption limit (Fanti et al. 1990, 1995). In our observations at resolution ~ 10 kpc, they would be seen as point-like steep-spectrum sources, as is indeed the case.

The main difference between compact steep spectrum sources and ERQs is that the former are in the unambiguously radio-loud regime, with radio luminosities between 10^{42} and 10^{44} erg s $^{-1}$ (Holt et al. 2008), two orders of magnitude larger than those of ERQs. One might argue that this difference reflects the selection of compact steep spectrum sources from radio surveys and hypothesize that ERQs are dominated by the lower power compact steep spectrum sources that had not been previously identified. We consider this possibility less likely on the basis of the radio distribution of ERQs. Many authors find that the radio properties of AGN populations are uncorrelated or weakly correlated with their

optical properties (Ivezić et al. 2002), which is reflected in the six orders of magnitude spread of radio luminosities within each subpopulation shown in Figure 5. It seems less likely that the optical and infrared selection criteria of ERQs would pick up weak compact steep spectrum jets so efficiently that they dominate the ERQ radio luminosity function while being subdominant in every other population, especially because low-power jets are not expected to be the dominant mode of outflow activity in near-Eddington sources (Jiang et al. 2014). Nonetheless we cannot completely exclude this possibility. The physical properties of ERQs are quite extreme and poorly understood, and perhaps the ERQ selection might somehow be biased toward compact jets. For example, high mid-infrared-to-optical ratio might tend to pick objects with extremely high gas and dust content, resulting in efficient confinement of jets and therefore hitting the ‘sweet spot’ for compact jet selection.

Another problem with the compact jet hypothesis is that the known compact jets do not fit in the tight correlation between radio luminosity and velocity width of ionized gas in Figure 7. Compact steep spectrum sources are known to be associated with high-velocity [O III] outflows produced as the jet interacts with the interstellar medium of the host galaxy. While the compact radio sources in Holt et al. (2008) are two orders of magnitude brighter in radio than ERQs, the full width at half maximum (FWHM) of [O III] spans widely from ~ 300 to 1500 km s^{-1} . In contrast, ERQs with existing [O III] observations frequently have high velocity widths of [O III] in excess of 2500 km s^{-1} while being radio-quiet, and they naturally lie on the extrapolation of the [O III] width versus radio relation found in other radio-quiet quasars (Zakamska & Greene 2014). Therefore, from kinematics, quasar-driven winds give a more natural explanation to the correlation.

Despite the wide range of radio luminosities observed in AGNs, there exists a correlation between the bolometric luminosity and the median radio luminosity which is characteristic of the radio-quiet population (White et al. 2007). This correlation has been interpreted as evidence that radio emission is due to low-power jets connected to accretion activity (Falcke et al. 1995). Continuing to explore the jet hypothesis, we turn to the spectral index which is used as a measure of the orientation of jets (Orr & Browne 1982; Richards et al. 2001). If a jet is viewed perpendicular to its axis, the optically thin synchrotron emission from the lobes and hotspots dominates the observed flux and makes the observed radio spectrum steep. Since the color selection of ERQs is designed to preferentially select obscured objects seen ‘edge-on’ in the classical unification model, we might expect to see steep spectra in jet-dominated ERQs.

Radio spectra can be further steepened by inverse

Compton scattering. At the redshifts of ERQs and on the scales of their host galaxy, the radiation field is dominated by the quasar rather than the commonly considered cosmic microwave background (Krolik & Chen 1991). Inverse-Compton losses in particular would affect low-radio-power sources more strongly than high-radio-power sources, which in the compact jet hypothesis might explain why radio-quiet ERQs have steeper spectra ($\alpha \lesssim -1.0$) than radio-loud broad absorption line quasars ($\alpha \simeq -0.7$; Becker et al. 2000; Richards et al. 2001). We find that the quasar radiation from ERQs is strong enough that inverse Compton scattering can be an important cooling source for the synchrotron-emitting particles (Nims et al. 2015), but its strong dependence on the magnetic field makes it difficult to quantify the effect at this time. The injection spectrum can also vary (Carilli et al. 1991), and in particular in some ultrastep-spectrum radio sources ($\alpha < -1$) the steepness may be due to a higher density environment into which jets propagate (Klamer et al. 2006; Bornciani et al. 2010). In short, the observed radio spectra of jets can be steepened by orientation, steep-spectrum injection, denser environment, rapid synchrotron and inverse-Compton cooling.

Observations with higher angular resolution could help distinguish compact jets from winds. However, despite dramatically different morphologies and launching mechanisms on scales near the black hole, these two scenarios are surprisingly difficult to disentangle on galaxy scales (Zakamska & Greene 2014; Harrison et al. 2015; Alexandroff et al. 2016). When a strongly collimated jet interacts with the dense interstellar medium of the host galaxy, it loses its directionality and on large scales it appears as an overpressured cocoon which continues to expand and sweep the surrounding medium (Begelman & Cioffi 1989), much like a wind.

Overall, we are not able to completely rule out compact jets as the origin of the ERQ radio emission. However, we find it unlikely that the optical and infrared selection criteria of ERQs would correlate so strongly with the presence of weak compact steep-spectrum jets, rare in other AGN populations. Furthermore, the compact jet hypothesis does not provide a quantitative explanation of the radio versus kinematics correlation presented in Figure 7. Although it is still possible that the ERQ selection hits the ‘sweet spot’ of weak compact jets, we find that by-product radio emission from winds is a more compelling explanation for the radio emission from ERQs.

5. CONCLUSIONS

Extremely red quasars are selected by their red optical-to-mid-infrared colors and high rest equivalent width of C IV (Ross et al. 2015; Hamann et al. 2017).

They are among the most powerful quasars in the Universe, with bolometric luminosities of $10^{47-48} \text{ erg s}^{-1}$, indicating that ERQs might be accreting at near- or super-Eddington levels. As many ERQs possess strong outflow signatures traced by ionized gas (Zakamska et al. 2016a; Perrotta et al. in prep.), ERQs serve as a natural population to explore the connection between radio emission and quasar-driven winds. In this paper, we present radio follow-up observations of 101 ERQs with VLA which we combine with detections in the FIRST survey. We present the following findings:

1. ~ 78 per cent of ERQs have radio luminosities between $10^{40} - 10^{42} \text{ erg s}^{-1}$ at 6 GHz, with a median of $1.1 \times 10^{41} \text{ erg s}^{-1}$. They have steep radio spectra with an average spectral index of $\alpha \sim -1.0$, and many individual objects have even steeper radio spectra. Except for SDSSJ1117+4623, which may be an $\sim 80 \text{ kpc}$ core+lobe system, no ERQ is resolved with a resolution of $\sim 10 \text{ kpc}$.
2. Based on radio morphology, we rule out large-scale jets as the origin of the radio emission in ERQs. We further rule out star formation as the dominant source of radio emission based on unrealistically high required star formation rates and unusually steep spectra of ERQs. Sub-parsec radio coronae and jet cores are also excluded due to their flat expected spectra.
3. ERQs tightly follow the correlation between the velocity width of [O III] and radio luminosity, first established in low-redshift type 2 quasars (Zakamska & Greene 2014), suggesting a strong connection between the galactic winds and the radio synchrotron emission. While we cannot completely rule out compact steep-spectrum jets as the origin of ERQs' radio emission, they do not provide a quantitative explanation for this relationship, whereas the observed radio emission can be naturally produced as a by-product of quasar-driven winds propagating into the host galaxy and shocking the surrounding interstellar medium (Jiang et al. 2010; Nims et al. 2015).

4. The wind scenario can explain the observed radio emission if the conversion from the bolometric luminosity to the kinetic power of the wind is ~ 1 per cent, consistent with other studies of quasar feedback. In this scenario radio spectra could be steep due to steep-spectrum injection or rapid cooling via synchrotron emission or inverse Compton scattering off a quasar's radiation field.
5. We see evidence that the radio luminosity function of AGNs includes at least three different contributions. All powerful, spatially resolved jet-powered radio sources are on the radio-loud end of the distribution, and the traditional radio-loudness definitions may be helpful in delineating this population. On the low-luminosity end, star formation in the host galaxy can make a dominant contribution. The nature of radio emission with luminosities $10^{39} - 10^{42} \text{ erg s}^{-1}$ remains ambiguous. The discovery of the relationship between radio emission and [O III] kinematics in type 2 quasars and ERQs in this range of luminosities suggests that galactic winds in powerful quasars can contribute radio emission in this intermediate regime.

The authors are grateful to R. White, S. van Velzen, and U. Rau for technical discussions, to the anonymous referee for constructive suggestions, and to the staff of the National Radio Astronomical Observatory for technical support and assistance with data storage and processing. HCH would also like to acknowledge the helpful discussion with Y.-K. Chiang, A.-L. Sun, and K. Hall. NLZ is grateful to Johns Hopkins University for support via the Catalyst Award and to the Institute for Advanced Study for hospitality during multiple visits. RA is supported by a Postdoctoral Fellowship awarded by the Natural Science and Engineering Research Council of Canada. Support for this work was also provided in part by the National Aeronautics and Space Administration through Chandra Award Number GO6-17100X issued by the Chandra X-ray Observatory Center, which is operated by the Smithsonian Astrophysical Observatory for and on behalf of the National Aeronautics Space Administration under contract NAS8-03060.

REFERENCES

- Alam, S., Albareti, F. D., Allende Prieto, C., et al. 2015, *ApJS*, 219, 12
- Alexandroff, R. M., Zakamska, N. L., van Velzen, S., Greene, J. E., & Strauss, M. A. 2016, *MNRAS*, 463, 3056
- Alexandroff, R. M., Zakamska, N. L., Barth, A., et al. 2017, *MNRAS*, submitted
- Antonucci, R. 1993, *ARA&A*, 31, 473
- Becker, R. H., White, R. L., Gregg, M. D., et al. 2000, *ApJ*, 538, 72
- Becker, R. H., White, R. L., & Helfand, D. J. 1995, *ApJ*, 450, 559
- Begelman, M. C., & Cioffi, D. F. 1989, *ApJL*, 345, L21
- Bell, E. F. 2003, *ApJ*, 586, 794
- Blain, A. W., Smail, I., Ivison, R. J., Kneib, J.-P., & Frayer, D. T. 2002, *PhR*, 369, 111

- Blandford, R. D., & Königl, A. 1979, *ApJ*, 232, 34
- Bornancini, C. G., O’Mill, A. L., Gurovich, S., & Lambas, D. G. 2010, *MNRAS*, 406, 197
- Brusa, M., Bongiorno, A., Cresci, G., et al. 2015, *MNRAS*, 446, 2394
- Carilli, C. L., Perley, R. A., Dreher, J. W., & Leahy, J. P. 1991, *ApJ*, 383, 554
- Carniani, S., Marconi, A., Maiolino, R., et al. 2015, *A&A*, 580, A102
- Chapman, S. C., Blain, A. W., Smail, I., & Ivison, R. J. 2005, *ApJ*, 622, 772
- Condon, J. J., Cotton, W. D., Greisen, E. W., et al. 1998, *AJ*, 115, 1693
- Condon, J. J., Kellermann, K. I., Kimball, A. E., Ivezić, Z., & Perley, R. A. 2013, *ApJ*, 768, 37
- Crichton, D., Gralla, M. B., Hall, K., et al. 2016, *MNRAS*, 458, 1478
- Cutri, R. M., Wright, E. L., Conrow, T., et al. 2011, Technical reports, Explanatory Supplement to the WISE Preliminary Data Release Products
- Dawson, K. S., Schlegel, D. J., Ahn, C. P., et al. 2013, *AJ*, 145, 10
- de Vries, W. H., Hodge, J. A., Becker, R. H., White, R. L., & Helfand, D. J. 2007, *AJ*, 134, 457
- Eisenstein, D. J., Weinberg, D. H., Agol, E., et al. 2011, *AJ*, 142, 72
- Everett, J. E. 2005, *ApJ*, 631, 689
- Falcke, H., Koerding, E., & Markoff, S. 2004, *A&A*, 414, 895
- Falcke, H., Malkan, M. A., & Biermann, P. L. 1995, *A&A*, 298, 375
- Fan, L., Han, Y., Nikutta, R., Drouart, G., & Knudsen, K. K. 2016, *ApJ*, 823, 107
- Fanti, C., Fanti, R., Dallacasa, D., et al. 1995, *A&A*, 302, 317
- Fanti, R., Fanti, C., Schilizzi, R. T., et al. 1990, *A&A*, 231, 333
- Farrah, D., Petty, S., Connolly, B., et al. 2017, *ApJ*, 844, 106
- Faucher-Giguère, C. A., & Quataert, E. 2012, *MNRAS*, 425, 605
- Fiore, F., Feruglio, C., Shankar, F., et al. 2017, *A&A*, 601, A143
- Fossati, G., Maraschi, L., Celotti, A., Comastri, A., & Ghisellini, G. 1998, *MNRAS*, 299, 433
- Greene, J. E., Zakamska, N. L., & Smith, P. S. 2012, *ApJ*, 746, 86
- Hamann, F., Zakamska, N. L., Ross, N., et al. 2017, *MNRAS*, 464, 3431
- Harrison, C. M., Alexander, D. M., Mullaney, J. R., & Swinbank, A. M. 2014, *MNRAS*, 441, 3306
- Harrison, C. M., Thomson, A. P., Alexander, D. M., et al. 2015, *ApJ*, 800, 45
- Heckman, T. M., Miley, G. K., van Breugel, W. J. M., & Butcher, H. R. 1981, *ApJ*, 247, 403
- Helou, G., Soifer, B. T., & Rowan-Robinson, M. 1985, *ApJ*, 298, L7
- Hodge, J. A., Becker, R. H., White, R. L., Richards, G. T., & Zeimann, G. R. 2011, *AJ*, 142, 3
- Holt, J., Tadhunter, C. N., & Morganti, R. 2008, *MNRAS*, 387, 639
- Ibar, E., Ivison, R. J., Best, P. N., et al. 2010, *MNRAS*, 401, L53
- Ishibashi, W., Banerji, M., & Fabian, A. C. 2017, *MNRAS*, 469, 1496
- Ishibashi, W., & Courvoisier, T. J. L. 2011, *A&A*, 525, A118
- Ivezić, Ž., Menou, K., Knapp, G. R., et al. 2002, *AJ*, 124, 2364
- Jiang, Y. F., Ciotti, L., Ostriker, J. P., & Spitkovsky, A. 2010, *ApJ*, 711, 125
- Jiang, Y.-F., Stone, J. M., & Davis, S. W. 2014, *ApJ*, 796, 106
- Kellermann, K. I., Condon, J. J., Kimball, A. E., Perley, R. A., & Ivezić, Z. 2016, *ApJ*, 831, 168
- Kellermann, K. I., Sramek, R., Schmidt, M., Shaffer, D. B., & Green, R. 1989, *AJ*, 98, 1195
- Kimball, A. E., Kellermann, K. I., Condon, J. J., Ivezić, Z., & Perley, R. A. 2011, *ApJL*, 739, L29
- Klamer, I. J., Ekers, R. D., Bryant, J. J., et al. 2006, *MNRAS*, 371, 852
- Königl, A., & Kartje, J. F. 1994, *ApJ*, 434, 446
- Kratzer, R. M., & Richards, G. T. 2015, *AJ*, 149, 61
- Krolik, J. H., & Chen, W. 1991, *AJ*, 102, 1659
- La Franca, F., Melini, G., & Fiore, F. 2010, *ApJ*, 718, 368
- Laor, A., & Behar, E. 2008, *MNRAS*, 390, 847
- Leipski, C., Falcke, H., Bennert, N., & Huettemeister, S. 2006, *A&A*, 455, 161
- Leitherer, C., Schaerer, D., Goldader, J. D., et al. 1999, *ApJS*, 123, 3
- Liu, G., Zakamska, N. L., Greene, J. E., Nesvadba, N. P. H., & Liu, X. 2013, *MNRAS*, 436, 2576
- McMullin, J., Waters, B., Schiebel, D., Young, W., & Golap, K. 2007, in *Astronomical Data Analysis Software and Systems XVI*, ed. R. Shaw, F. Hill, & D. Bell, Vol. 376 (Astronomical Society of the Pacific (ASP)), 127
- Mullaney, J. R., Alexander, D. M., Fine, S., et al. 2013, *MNRAS*, 433, 622
- Murphy, E. J. 2013, *ApJ*, 777, 58
- Murphy, E. J., Condon, J. J., Schinnerer, E., et al. 2011, *ApJ*, 737, 67
- Murphy, E. J., Bremseth, J., Mason, B. S., et al. 2012, *ApJ*, 761, 97
- Murray, N., Chiang, J., Grossman, S. A., & Voit, G. M. 1995, *ApJ*, 451, 498
- Murray, N., Quataert, E., & Thompson, T. A. 2005, *ApJ*, 618, 569
- Nims, J., Quataert, E., & Faucher-Giguere, C.-A. 2015, *MNRAS*, 447, 3612
- Obied, G., Zakamska, N. L., Wylezalek, D., & Liu, G. 2016, *MNRAS*, 456, 2861
- Orr, M. J. L., & Browne, I. W. A. 1982, *MNRAS*, 200, 1067
- Pâris, I., Petitjean, P., Aubourg, É., et al. 2014, *A&A*, 563, A54
- Pâris, I., Petitjean, P., Ross, N. P., et al. 2017, *A&A*, 597, A79
- Perna, M., Brusa, M., Cresci, G., et al. 2015, *A&A*, 574, A82
- Proga, D., & Kallman, T. R. 2004, *ApJ*, 616, 688
- Proga, D., Stone, J. M., & Kallman, T. R. 2000, *ApJ*, 543, 686
- Rafter, S. E., Crenshaw, D. M., & Wiita, P. J. 2009, *AJ*, 137, 42
- Raginski, I., & Laor, A. 2016, *MNRAS*, 459, 2082
- Rau, U., Bhatnagar, S., & Owen, F. N. 2016, *AJ*, 152, 124
- Rau, U., & Cornwell, T. J. 2011, *A&A*, 532, A71
- Rawlings, J. I., Page, M. J., Symeonidis, M., et al. 2015, *MNRAS*, 452, 4111
- Reyes, R., Zakamska, N. L., Strauss, M. A., et al. 2008, *ApJ*, 136, 2373
- Richards, G. T., Laurent-Muehleisen, S. A., Becker, R. H., & York, D. G. 2001, *ApJ*, 547, 635
- Richards, G. T., Lacy, M., Storrie-Lombardi, L. J., et al. 2006, *ApJS*, 166, 470
- Rieke, G. H., Alonso-Herrero, A., Weiner, B. J., et al. 2009, *ApJ*, 692, 556
- Rosario, D. J., Burtscher, L., Davies, R. I., et al. 2013, *ApJ*, 778, 94
- Ross, N. P., Hamann, F., Zakamska, N. L., et al. 2015, *MNRAS*, 453, 3932
- Rupke, D., Gültekin, K., & Veilleux, S. 2017, *ArXiv e-prints*, arXiv:1708.05139
- Seaquist, E. R., & Odegard, N. 1991, *ApJ*, 369, 320
- Spitkovsky, A. 2008, *ApJL*, 682, L5
- Stocke, J. T., Morris, S. L., Weymann, R. J., & Foltz, C. B. 1992, *ApJ*, 396, 487
- Sun, A.-L., Greene, J. E., & Zakamska, N. L. 2017, *ApJ*, 835, 222
- Thompson, T. A., Fabian, A. C., Quataert, E., & Murray, N. 2015, *MNRAS*, 449, 147

- Urry, C. M., & Padovani, P. 1995, *PASP*, 107, 803
- van Velzen, S., Falcke, H., & Koerding, E. 2015, *MNRAS*, 446, 2985
- Wang, J.-M. 2008, *ApJL*, 682, L81
- Wang, R., Momjian, E., Carilli, C. L., et al. 2017, *ApJL*, 835, L20
- White, R. L., Becker, R. H., Helfand, D. J., & Gregg, M. D. 1997, *ApJ*, 475, 479
- White, R. L., Helfand, D. J., Becker, R. H., Glikman, E., & de Vries, W. 2007, *ApJ*, 654, 99
- White, R. L., Becker, R. H., Gregg, M. D., et al. 2000, *ApJS*, 126, 133
- White, S. V., Jarvis, M. J., Kalfountzou, E., et al. 2017, *MNRAS*, 468, 217
- Wright, E. L., Eisenhardt, P. R. M., Mainzer, A., et al. 2010, *AJ*, 140, 1868
- Xu, C., Livio, M., & Baum, S. A. 1999, *ApJ*, 118, 1169
- Zakamska, N. L., & Greene, J. E. 2014, *MNRAS*, 442, 784
- Zakamska, N. L., Strauss, M. A., Heckman, T. M., Ivezić, Z., & Krolik, J. H. 2004, *AJ*, 128, 1002
- Zakamska, N. L., Strauss, M. A., Krolik, J. H., et al. 2006, *AJ*, 132, 1496
- Zakamska, N. L., Hamann, F., Pâris, I., et al. 2016a, *MNRAS*, 459, 3144
- Zakamska, N. L., Lampayan, K., Petric, A., et al. 2016b, *MNRAS*, 455, 4191
- Zubovas, K., & King, A. 2012, *ApJL*, 745, L34

Table 1. FIRST detections of ERQs.

Source name	z^a	$F_{\nu,P}^b$	$F_{\nu,I}^c$	L_{radio}^d	targeting ^e
SDSSJ082653.42+054247.3	2.573	1.14	0.9	7.10E+41	
SDSSJ083200.20+161500.3	2.447	1.00	1.13	7.98E+41	
SDSSJ091508.45+561316.0	2.859	1.19	1.29	1.28E+42	radio-only
SDSSJ095033.51+211729.1	2.745	1.52	1.01	9.19E+41	radio-only
SDSSJ095823.14+500018.1	2.375	10.33	10.72	7.09E+42	
SDSSJ102447.32-013633.8	2.876	9.31	9.55	9.64E+42	
SDSSJ102541.78+245424.2	2.571	1.27	0.60	4.01E+41	
SDSSJ155057.71+080652.1 ^f	2.514	1.28	2.36	1.77E+42	
SDSSJ164725.72+522948.6	2.719	1.17	1.14	1.02E+42	
SDSSJ165202.64+172852.3	2.942	1.64	1.26	1.34E+42	

^aEmission-line redshift from DR12Q.

^bPeak flux density observed at 1.4 GHz in mJy beam⁻¹ in the FIRST catalog.

^cIntegrated flux density observed at 1.4 GHz in mJy in the FIRST catalog.

^dRadio luminosity νL_ν at rest-frame 6 GHz in erg s⁻¹.

^eIf a source is marked as radio-only, it is targeted for follow-up SDSS spectroscopy only because of its radio emission detected by FIRST. Radio-only ERQs are excluded from the statistical analysis in the paper.

^fERQ-like object.

Table 2. Tests of flux density measurement for artificial point sources, as described in Section 2.3.

$F_{\nu,expected}^a$	$F_{\nu,max}^b$	$F_{\nu,I,sky}^c$	$F_{\nu,P,sky}^d$	$F_{\nu,I}^e$	$F_{\nu,P}^f$
50	58.0 ± 5.9	61.9 ± 17.6	53.4 ± 7.5	78.9 ± 12.5	55.9 ± 6.0
100	106.9 ± 6.1	107.7 ± 16.5	101.3 ± 7.2	128.6 ± 11.1	103.4 ± 6.5
200	205.6 ± 6.1	204.2 ± 14.4	200.7 ± 7.0	228.1 ± 10.6	201.8 ± 6.9

^aThe expected flux density for the artificial point source in μ Jy.

^bMaximum pixel intensity of a source in μ Jy beam⁻¹.

^cFitted integrated flux density with consideration of the sky level in μ Jy.

^dFitted peak flux density with consideration of the sky level in μ Jy beam⁻¹.

^eFitted integrated flux density without consideration of the sky level in μ Jy.

^fFitted peak flux density without consideration of the sky level in μ Jy beam⁻¹.

Table 3. Spectral Indices, in the order of radio luminosity.

Source name	ERQ type	L_{radio}^a	$\alpha_{outband}$	α_{MFS}	α_{inband}
SDSSJ1117+4623	main	1.9E42	0.17 ± 0.10	0.29 ± 0.15	0.37 ± 0.09
SDSSJ0209+3122	main	8.1E41	– ^b	-1.86 ± 0.39	-1.89 ± 0.24
SDSSJ1550+0806	like	7.0E41	-1.02 ± 0.07	-1.27 ± 0.27	-1.80 ± 0.72
SDSSJ0220+0137	main	6.2E41	-0.59 ± 0.23	-1.07 ± 0.24	-1.12 ± 0.25
SDSSJ1145+5742	like	5.2E41	-0.97 ± 0.13	-1.15 ± 0.17	-0.72 ± 0.60
SDSSJ1301+1312	main	4.3E41	-1.13 ± 0.12	-0.76 ± 0.20	-1.44 ± 0.27
SDSSJ1451+2338	like	4.1E41	-1.07 ± 0.12	-1.31 ± 0.36	-1.31 ± 0.21
SDSSJ2215–0056 ^c	main	1.8E41	-1.00 ± 0.11	–	–
Average (80 – 150 μ Jy)	–	2.3E41	-0.92 ± 0.30	–	-1.08 ± 0.25
Average (< 80 μ Jy)	–	9.9E40	-1.04 ± 0.44	–	-1.35 ± 0.34

^aRadio luminosity νL_ν at rest-frame 6 GHz in erg s^{-1} .

^bNot covered by FIRST.

^cDetected in Stripe 82.

Table 4. Radio flux densities and luminosities of ERQs.

Source name	ERQ type ^a	z^b	F_ν^c	L_{radio}^d
SDSSJ000610.67+121501.2	main	2.310	82 ± 12	1.45E+41
SDSSJ000746.19+122223.9	main	2.429	39 ± 7	7.73E+40
SDSSJ001120.22+260109.2	like	2.290	64 ± 8	1.11E+41
SDSSJ002400.25+245031.9	main	2.809	40 ± 8	1.10E+41
SDSSJ003747.98+170504.0	like	3.664	47 ± 8	2.27E+41
SDSSJ004713.21+264024.7	main	2.564	49 ± 8	1.09E+41
SDSSJ005044.95-021217.6	main	2.254	< 29	<4.88E+40
SDSSJ005233.24-055653.5	main	2.354	134 ± 8	2.47E+41
SDSSJ014111.13-031852.5	main	2.559	45 ± 8	9.93E+40
SDSSJ015222.58+323152.7	main	2.786	< 27	<7.20E+40
SDSSJ020932.15+312202.7	main	2.376	429 ± 8	8.06E+41
SDSSJ022052.11+013711.1	main	3.138	199 ± 7	6.91E+41
SDSSJ080425.75+470159.0	main	2.772	< 47	<1.25E+41
SDSSJ080547.66+454159.0	main	2.326	62 ± 8	1.11E+41
SDSSJ082536.31+200040.3	main	2.094	< 30	<4.32E+40
SDSSJ082508.77+355822.9	like	2.894	63 ± 8	1.83E+41
SDSSJ082649.30+163945.2	main	2.316	< 29	<5.24E+40
SDSSJ083448.48+015921.1	main	2.594	83 ± 8	1.90E+41
SDSSJ084447.66+462338.7	main	2.217	103 ± 8	1.66E+41
SDSSJ084424.50+545234.2	like	2.702	34 ± 8	8.50E+40
SDSSJ085451.11+173009.1	main	2.614	< 32	<7.48E+40
SDSSJ090306.18+234909.8	main	2.263	< 32	<5.47E+40
SDSSJ091303.90+234435.2	main	2.420	50 ± 9	9.72E+40
SDSSJ092049.59+282200.9	main	2.296	< 32	<5.60E+40
SDSSJ093226.93+461442.8	main	2.314	53 ± 9	9.31E+40
SDSSJ093506.96-024137.7	main	2.167	< 36	<5.56E+40
SDSSJ093638.41+101930.3	main	2.453	< 53	<1.07E+41
SDSSJ093926.67+591311.1	like	3.744	< 30	<1.52E+41
SDSSJ101324.53+342702.6	main	2.482	52 ± 10	1.08E+41
SDSSJ101326.23+611219.9	like	3.703	101 ± 7	4.98E+41
SDSSJ101533.65+631752.6	main	2.226	< 32	<5.12E+40
SDSSJ102130.74+214438.4	main	2.194	35 ± 8	5.52E+40
SDSSJ102353.44+580004.9	main	2.597	23 ± 6	5.36E+40
SDSSJ103146.53+290324.1	main	2.293	61 ± 7	1.06E+41
SDSSJ103456.95+143012.5	main	2.961	65 ± 8	1.98E+41
SDSSJ104611.50+024351.6	main	2.773	88 ± 7	2.32E+41
SDSSJ104718.35+484433.8	main	2.275	< 28	<4.73E+40
SDSSJ104754.58+621300.5	main	2.536	48 ± 7	1.05E+41
SDSSJ110202.68-000752.7	main	2.626	< 32	<7.40E+40
SDSSJ111017.13+193012.5	main	2.505	42 ± 7	8.85E+40
SDSSJ111346.10+185451.9	main	2.516	< 27	<5.68E+40

Table 4 continued

Table 4 (*continued*)

Source name	ERQ type ^a	z^b	F_ν^c	L_{radio}^d
SDSSJ111355.72+451452.6	main	2.188	109 ± 7	1.70E+41
SDSSJ111516.33+194950.4	main	2.792	< 27	<7.22E+40
SDSSJ111729.56+462331.2	main	2.132	1266 ± 7	1.87E+42
SDSSJ113349.71+634740.0	main	2.202	122 ± 7	1.94E+41
SDSSJ113834.68+473250.0	main	2.310	47 ± 7	8.27E+40
SDSSJ114508.00+574258.6	like	2.790	145 ± 7	3.88E+41
SDSSJ114855.47+572159.8	like	3.054	< 28	<9.02E+40
SDSSJ121704.70+023417.1	main	2.416	30 ± 7	5.92E+40
SDSSJ122000.68+064045.3	main	2.796	< 28	<7.43E+40
SDSSJ123241.73+091209.3	main	2.381	37 ± 7	7.05E+40
SDSSJ124106.97+295220.8	main	2.794	34 ± 7	9.12E+40
SDSSJ124738.40+501517.7	main	2.386	42 ± 7	8.06E+40
SDSSJ125019.46+630638.6	main	2.402	28 ± 7	5.30E+40
SDSSJ125449.50+210448.4	main	3.118	33 ± 7	1.14E+41
SDSSJ125811.25+212359.6	main	2.614	36 ± 8	8.34E+40
SDSSJ130114.46+131207.4	main	2.787	147 ± 7	3.92E+41
SDSSJ130421.12+083752.2	main	2.946	162 ± 30	4.88E+41
SDSSJ130654.76+132704.8	main	2.499	60 ± 7	1.26E+41
SDSSJ130630.66+584734.7	main	2.297	28 ± 8	4.86E+40
SDSSJ130936.14+560111.3	main	2.569	50 ± 16	1.12E+41
SDSSJ131047.78+322518.3	main	3.017	55 ± 29	1.76E+41
SDSSJ131722.85+322207.5	main	2.400	33 ± 8	6.39E+40
SDSSJ131833.76+261746.9	main	2.272	21 ± 7	3.55E+40
SDSSJ134026.99+083427.2	main	2.483	50 ± 8	1.04E+41
SDSSJ134001.90+322155.9	main	2.405	< 30	<5.85E+40
SDSSJ134450.51+140139.2	main	2.745	< 32	<8.40E+40
SDSSJ134417.34+445459.4	main	3.036	< 90	<2.89E+41
SDSSJ134535.66+600028.4	main	2.937	< 26	<7.86E+40
SDSSJ135557.60+144733.1	main	2.704	< 29	<7.25E+40
SDSSJ135608.32+073017.2	main	2.269	< 34	<5.74E+40
SDSSJ140506.80+543227.3	main	3.213	68 ± 8	2.48E+41
SDSSJ141350.76+214307.7	main	2.440	< 27	<5.47E+40
SDSSJ143159.76+173032.6	main	2.377	< 39	<7.36E+40
SDSSJ144742.66+565209.2	like	2.789	97 ± 7	2.58E+41
SDSSJ145113.61+013234.1	like	2.773	58 ± 8	1.53E+41
SDSSJ145148.01+233845.4	like	2.621	167 ± 7	3.90E+41
SDSSJ145354.70+190343.9	main	2.349	87 ± 10	1.59E+41
SDSSJ145623.35+214516.2	main	2.476	80 ± 12	1.65E+41
SDSSJ150117.07+231730.9	main	3.025	< 39	<1.26E+41
SDSSJ152941.01+464517.6	main	2.420	< 43	<8.38E+40
SDSSJ153107.14+105825.8	main	2.781	< 32	<8.51E+40
SDSSJ153108.10+213725.1	main	2.569	< 34	<7.60E+40
SDSSJ153446.26+515933.8	main	2.265	80 ± 9	1.36E+41

Table 4 *continued*

Table 4 (*continued*)

Source name	ERQ type ^a	z^b	F_ν^c	L_{radio}^d
SDSSJ154243.87+102001.5	main	3.215	47 ± 8	1.70E+41
SDSSJ154523.97+165054.2	like	2.954	< 32	$< 9.85E+40$
SDSSJ154743.78+615431.1	main	2.868	57 ± 10	1.61E+41
SDSSJ154831.92+311951.4	main	2.736	40 ± 9	1.02E+41
SDSSJ155057.71+080652.1	like	2.514	266 ± 8	5.67E+41
SDSSJ160431.55+563354.2	main	2.484	62 ± 8	1.29E+41
SDSSJ162920.36+495705.3	like	2.759	93 ± 8	2.44E+41
SDSSJ170558.64+273624.7	main	2.448	34 ± 7	6.88E+40
SDSSJ171420.38+414815.7	main	2.342	42 ± 8	7.64E+40
SDSSJ220337.79+121955.3	main	2.623	102 ± 29	2.38E+41
SDSSJ221524.00-005643.8	main	2.509	98 ± 7	2.09E+41
SDSSJ222421.63+174041.2	main	2.165	< 28	$< 4.31E+40$
SDSSJ223754.52+065026.6	main	2.609	< 28	$< 6.44E+40$
SDSSJ225438.30+232714.5	main	3.087	< 28	$< 9.47E+40$
SDSSJ232326.17-010033.1	main	2.356	< 34	$< 6.31E+40$
SDSSJ232828.47+044346.8	main	2.564	< 48	$< 1.05E+41$
SDSSJ233636.99+065231.0	main	2.776	54 ± 7	1.44E+41

^a‘Main’ sources are refer to ERQs in this paper, and to ‘core’ ERQs in [Hamann et al. \(2017\)](#). ‘Like’ sources are ERQ-like objects in both [Hamann et al. \(2017\)](#) and this paper.

^bEmission-line redshift from DR12Q.

^cFlux density observed at 6.2 GHz in μJy . Flux density error is the root-mean-square noise of each field based on the test in Section 2.3.

^dRadio luminosity νL_ν at rest-frame 6 GHz in erg s^{-1} .